UNIVERSITAT POLITÈCNICA DE VALÈNCIA

_ TELECOM ESCUELA TÉCNICA VLC SUPERIOR DE INGENIERÍA DE TELECOMUNICACIÓN

UNIVERSITAT POLITÈCNICA DE VALÈNCIA

School of Telecommunications Engineering

Demonstration of ultra-low-loss electro-optical switches in silicon nitride technology

Master's Thesis

Master's Degree in Telecommunication Engineering

AUTHOR: Ribera Vicent, Miguel

Tutor: Sanchis Kilders, Pablo

Experimental director: PARRA GOMEZ, JORGE

ACADEMIC YEAR: 2021/2022

UNIVERSITAT POLITÈCNICA DE VALÈNCIA

_ TELECOM ESCUELA TÉCNICA VLC SUPERIOR DE UPV INGENIEROS DE TELECOMUNICACIÓN

Demonstration of ultra-low-loss electro-optical switches in silicon nitride technology

Author:	Miguel Ribera Vicent
Supervisor:	Pablo Sanchis Kilders
Co-Supervisor:	Jorge Parra Gómez

Master's Thesis presented at Escuela Técnica Superior de Ingeniería de Telecomunicación of Universitat Politècnica de València, to obtain the title "Máster Universitario en Ingeniería de Telecomunicación".

Course 2021-22

Valencia, July 9, 2022

Agradecimientos

Desde estas líneas quiero agradecer el apoyo recibido, a todas las personas que han estado a mi lado a lo largo de estos años, gracias a las cuales ha sido posible mi desarrollo tanto académico como personal.

En especial agradecer a mis padres por haberme brindado la oportunidad de estudiar con la tranquilidad de saber que cuento con su respaldo. También a mis familiares más cercanos y amigos, por su apoyo incondicional y sus consejos. Y por supuesto, a los directores de mi trabajo, Pablo y Jorge, gracias por guiarme en este proyecto y estar ahí siempre que lo he necesitado.

Gracias.

Resumen

El objetivo del trabajo fin de máster es la demostración experimental y análisis de prestaciones de conmutadores electro-ópticos integrados en tecnología de nitruro de silicio. La tecnología de nitruro de silicio elegida permite unas pérdidas ultra-bajas que son cruciales para el ámbito de aplicación de los conmutadores que se pretenden demostrar. Concretamente, el conmutador es un elemento funcional de un sistema que permite llevar a cabo un conformado óptico de haces en radares de apertura sintética para aplicaciones satelitales. Inicialmente, se realizará un estudio teórico para evaluar los parámetros más significativos del conmutador y su impacto en las prestaciones. A continuación, se llevará a cabo la caracterización de prototipos experimentales y medida de sus prestaciones.

Resum

L'objectiu del treball fi de màster és la demostració experimental i anàlisi de prestacions de commutadors electro-òptics integrats en tecnologia de nitrur de silici. La tecnologia de nitrur de silici triada permet unes pèrdues ultres-baixes que són crucials per a l'àmbit d'aplicació dels commutadors que es pretenen demostrar. Concretament, el commutador és un element funcional d'un sistema que permet dur a terme un conformat òptic de feixos en radars d'obertura sintètica per a aplicacions satel·litàries. Inicialment, es realitzarà un estudi teòric per a avaluar els paràmetres més significatius del commutador i el seu impacte en les prestacions. A continuació, es durà a terme la caracterització de prototips experimentals i mesura de les seves prestacions.

Abstract

The aim of the master's thesis is the experimental demonstration and performance analysis of integrated electro-optical switches in silicon nitride technology. The chosen silicon nitride technology allows ultra-low losses that are crucial for the application of the components to be demonstrated. Specifically, the switch is a functional element of a system that enables optical beamforming to be carried out in synthetic aperture radars for satellite applications. Initially, a theoretical study will be realised to evaluate the most significant parameters of the switch and their impact on performance. Then, the characterisation of experimental prototypes and measurement of their performance will be carried out.

Contents

List of Figures

List of Tables

Chapter 1

Introduction

1.1 Motivation

1.1.1 Introduction

The world of communication technologies has been undergoing significant changes for decades. As time goes by, more and more components are being integrated into the same device to achieve more complex functionalities in as small a space as possible. Research fields such as photonics have experienced such an essential boom in recent years, as they can provide higher bandwidths than electronics. Therefore, it is increasingly common to see devices that combine electronics and photonics on the same platforms, bringing together two worlds that complement each other. This combination of optical communication technology and electronic circuits enables high-speed transmissions between mobile devices, high-speed communication without data centres, new sensor systems and many other applications. Thereby, light transmission systems cover the entire spectrum of high-speed communication, from long-distance systems such as transoceanic links to short-distance systems connections in data centres and optical connections on the chip, [1], [2].

Therefore, photonics is increasingly present in more and more of our everyday applications, becoming increasingly indispensable to us. Hence, integrating it into progressively compact circuits that offer a wide variety of functionalities with the lowest possible power consumption. Therefore, it is clear that photonic integrated circuits (PIC)s are a leading topic in technology and innovation for many tech companies and research centres around the world. And although photonics technology is still a long way from reaching the maturity of electronics, the growth of the market in this field suggests that it will reach an unprecedented level in less time than expected [3]. So it can be said that the complexity of photonic integration has been dramatically ameliorated and expanded in the last years. It enables a wide range of applications, from telecommunications and data communication to sensors such as gyroscopes, biosensors, spectrometers and light detection and ranging (LiDAR) [4].

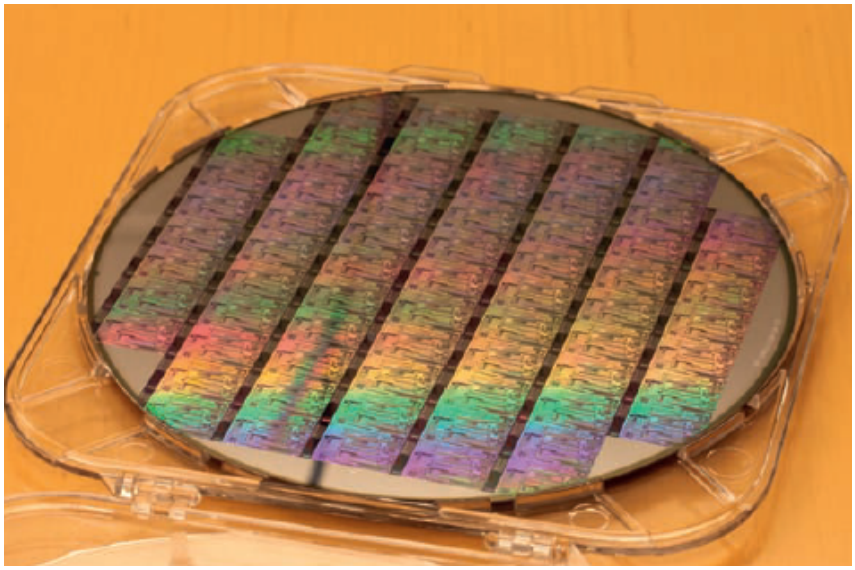

Figure 1.1: Photograph of 8" SOI wafer with various photonic components and circuits [1].

1.1.2 Photonic Integrated Circuits

Within the field of integrated photonic circuits, there are several established platforms or technologies that are more or less appropriate depending on the applications and components to be developed. These technologies are based on the main material of the waveguide used in each case and are mainly silicon photonics, silicon nitride, and indium phosphide. In this work, we will deal with the first two mentioned since silicon photonics is the most developed to date and silicon nitride is the one we are working on in this project.

Silicon photonics

Integrated photonics has been an essential pass to follow the electronics steps to add more and more functionalities in a smaller space. To achieve this in both disciplines, silicon is fundamental as it is able to combine photonics and electronics on a single platform. Silicon is a well-researched and robust material whose strong optical confinement enables device scaling to hundreds of nanometres due to the high index contrast between SiO_2 (n = 1.45) and silicon (n = 3.45). In addition, the bandgap of silicon is about 1.1 eV, making the material transparent to the wavelengths 1.3 μm to 1.6 μm commonly used in optical communications. Furthermore, the fabrication processes found in the microelectronics industry can be utilize for developing silicon-based integrated photonic circuits. Thus, the silicon photonic technology becomes potentially cheap and scalable. This makes photonics based on silicon the major active discipline within integrated optics these days, [1], [5], [6]. One of the keys to the long-term success of the microelectronics community has been the emergence of complementary metal-oxide-semiconductor (CMOS) technology, which has enabled embeddedness into a very large scale integration (VLSI) system. This integration has led to the great success of today's silicon integrated circuits (ICs). By making these mass production processes publicly available for research and development at

a modest cost, anyone with very fair means can do cutting-edge creative work in a process that can be immediately produced at a large scale [1], [5].

Optical communication is the mainstream application of silicon photonics. Nonetheless, a large number of applications proposed by research centres and universities have come forward [7]. Today, standard silicon photonics products are manufactured on silicon-on-insulator (SOI) wafers, which has developed into a sophisticated technology that enables the generation, modulation and detection of optical signals on-chip through heterogeneous or hybrid integration of different materials. These wafers are based on a crystalline silicon layer resting on a silicon oxide buffer layer forms the core layer from which a wide variety of waveguide-based devices can be patterned [8], [9]. For a PIC, Si can provide low-loss waveguides that interconnect various photonic elements that perform specific functions, including lasers, modulators, photodetectors, and other passive devices as phase tuners, arrayed waveguide gratings (AWGs), Mach-Zehnder interferometer (MZI), etc. The number of devices on a single Si-PIC increases thanks to the high yield of devices and the application requirements for large-format PICs in areas such as high-speed transceivers, optical data processing, LiDAR and quantum photonics. In Fig. 1.2, the evolution of the number of photonic devices integrated on a single waveguide for platforms including monolithic InP, monolithic Si, and heterogeneous InP/Si or GaAs/Si is summarised [4].

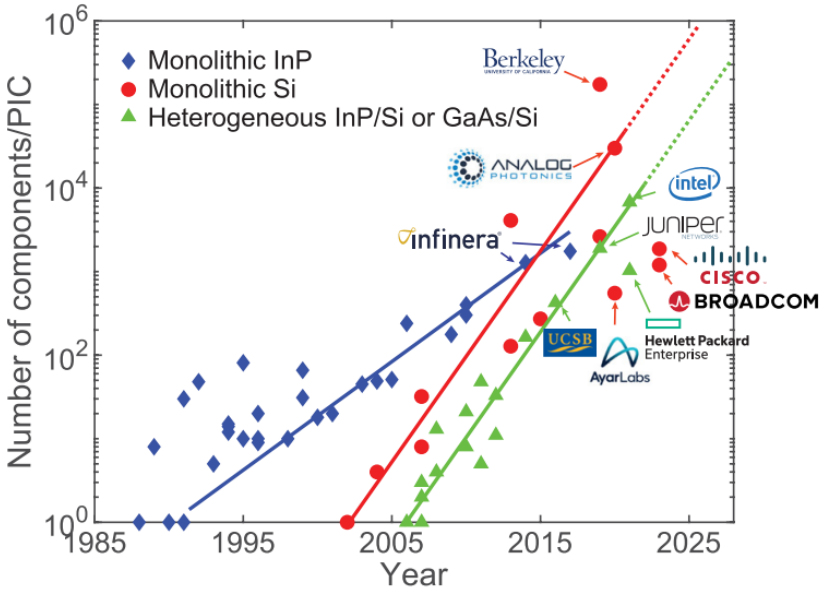

Figure 1.2: The number of photonic components integrated on a single waveguide over time for three photonic integration platforms: InP substrate with integrated lasers, Si substrate without integrated lasers, and Si substrate with integrated lasers [4].

In spite of all benefits which SOI technology presents for photonics, especially, for passive structures. This platform also exhibits some drawbacks in terms of light generation at any band and light detection, especially in the telecommunication band. It also lacks second-order optical non-linearity and suffers from non-linear absorption when its third-order optical non-linearity is exploited. This has encouraged the heterogeneous integration of other materials ranging from

III-V compound semiconductors to second and third-order non-linear optical materials (e.g., lithium niobate, silicon nitride, highly refractive non-linear glasses or metal oxides) on silicon substrates [10].

However, it is clear that despite these shortcomings, Si still reigns supreme in the world of photonics. New applications in this field are appearing all the time, e.g., the company *KVH* released fiber optical gyroscopes (FOG) based on silicon photonics, intended for robotic car navigation. Also, *Genalyte* released systems for immunoassays based on silicon photonics elements. Another notable milestone would be the American company *Rockley Photonics* which announced its intention to participate in a new challenge with an initial valuation of 1.2 B$ with an Apple-supported spectrophotometer project for smartwatches. Apart from these landmarks, there are other new applications to highlight, e.g. the frequency modulated continuous wave (FMCW) for LiDAR in order to serve autonomous driving, or others like electronic noses, optical coherence tomography (OCT), and cardiovascular diagnostic devices [7]. Therefore, a very promising market is foreseen for the coming years. In Fig. 1.3 the relevance of the main applications of silicon photonics in the coming years is presented in economic terms.

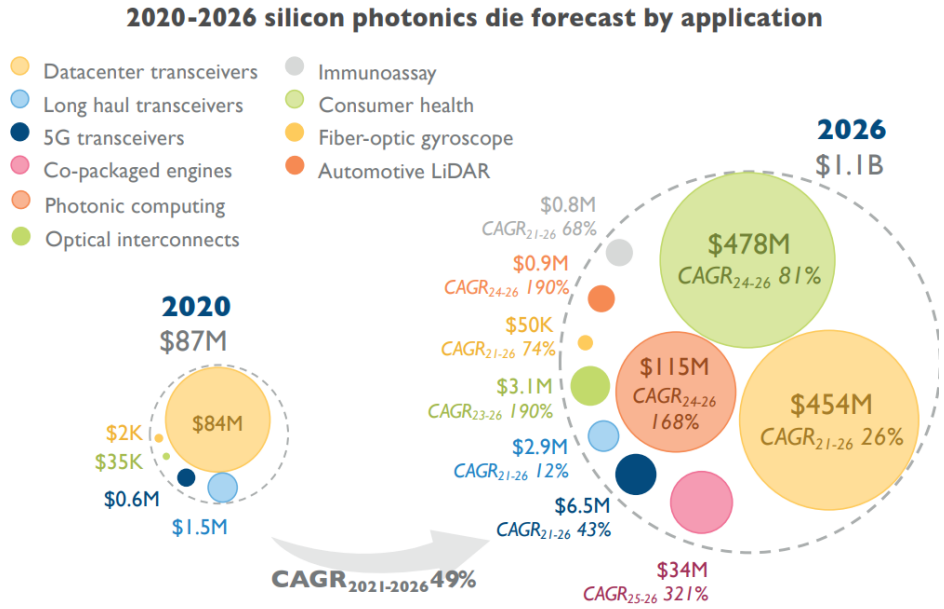

Figure 1.3: 2020-2026 silicon photonics die forecast by application, [7].

Silicon nitride platform

While the SOI approach has gained acceptance in silicon photonics, there is increasing interest in researching alternative material combinations that share the same essential properties as SOI: high index contrast and CMOS compatibility. And this is where silicon nitride comes in, so it is a common material in CMOS industry. It is usually produced by low-pressure chemical vapour deposition (LPCVD) at high temperatures (> 700) ^{o}C. The main benefits of Si_3N_4 compared to Si is its transparency from visible to mid-infrared wavelengths, the absence of two-photon absorption, the strong Kerr non-linearity, and a high refractive index [8], [9].

Talking about the transparency range, SOI waveguides only have low absorption losses in the range from 1.1 μm to 3.7 μm while the same structures based on Si_3N_4, can operate down to at least 500 nm [8]. So are able to data communication at 850 nm [9]. On the other hand, the moderate index contrast of Si_3N_4 waveguide highly reduces the optical losses due to sidewalls roughness compared to the Si counterparts. In such a way, ultralow-losses of around 1 dB/m can be achieved with Si_3N_4, which a reduction of two orders of magnitude in comparison with Si ($\sim$ 1 dB/cm) [8]. In Fig. 1.4 a comparison of waveguide propagation loss, minimum bend radius, and wavelength operation range between the most used technologies in photonics as SOI and Si_3N_4 waveguides, are carried out [11].

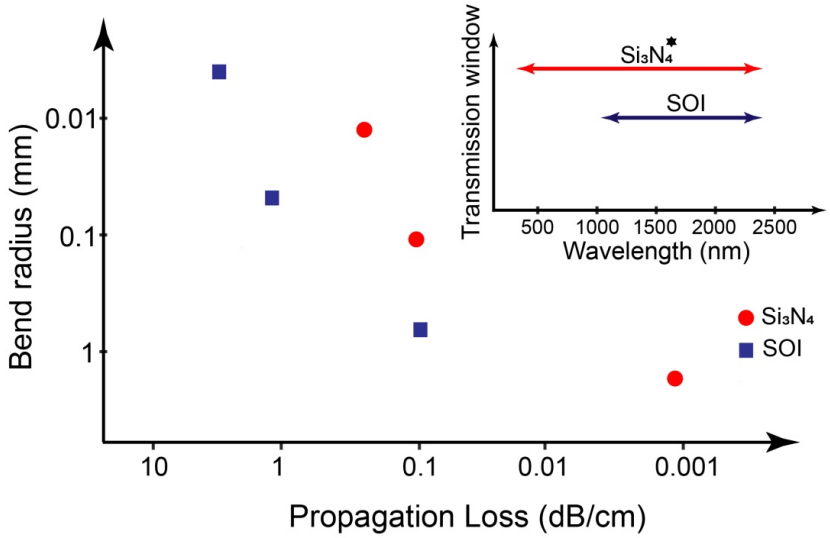

Figure 1.4: Bend radius, propagation loss, and window of transparency for published Si_3N_4 and SOI waveguides [11].

This broad spectrum of Si_3N_4 technology allows it to have a range of applications from infrared (IR) down through the mid-infrared (MIR), near-infrared (NIR), and visible. Covering a wide range of application areas, including telecommunications, sensing, biophotonics etc [11]. In visible light spectrum (400 - 700 nm) Si_3N_4 is a highly efficient platform for integrated photonics applications. In [12], amazingly low loss performance is demonstrated in waveguide bends, grating couplers and multimode interference (MMI) couplers at the 660 nm wavelength. Si_3N_4 also is interesting in NIR (700 - 1000 nm), so it complements the possibilities of SOI photonics [11]. According to [8] Si_3N_4 has comparatively negligible two-photon absorption in this range, and despite its Kerr non-linear being smaller, this has enabled Si_3N_4 as a crucial platform for non-linear applications, such as supercontinuum and frequency comb generation. All these features leads in these ranges, NIR and visible, to reach applications such as quantum communication and computation, LiDAR, free-space communications, atomic physics, sensing and spectroscopy, astronomy, biophotonics etc. In the field of IR range (1000 - 2300 nm) Si_3N_4 takes advantage of transparency, low losses, and the ability to package this technology circuits with SOI and InP. Applications in this range include optical filters, delay lines, lasers, microwave synthesizers, optical inertial rotation sensors, quantum communications, real-time delays, optical signal processors, etc [11], [13].

Silicon photonics, SOI and silicon nitride, in particular, has outlined their value proposition in the ability to design and manufacture a system-on-chip (SoC) with a high technology readiness level (TRL). Fortunately, here in Europe, we have a consolidated ecosystem capable of covering from the design of a first idea to the fabrication and testing of a functional system in integrated photonics [14]. Public and private investment in research and development has led to the rapid growth of silicon photonics technologies over the past two decades. Even for modest quantities of production, the cost-effectiveness of silicon photonics is exploited with CMOS electronics manufacturing. The open-access foundry model is one of the success stories of semiconductor electronics. This open-access model enables an economically viable and low-barrier access to fabless companies where such companies bank on the off-the-shelf intellectual property (IP) and technology processes of pure-play foundries for PIC prototyping and manufacturing [14], [15].

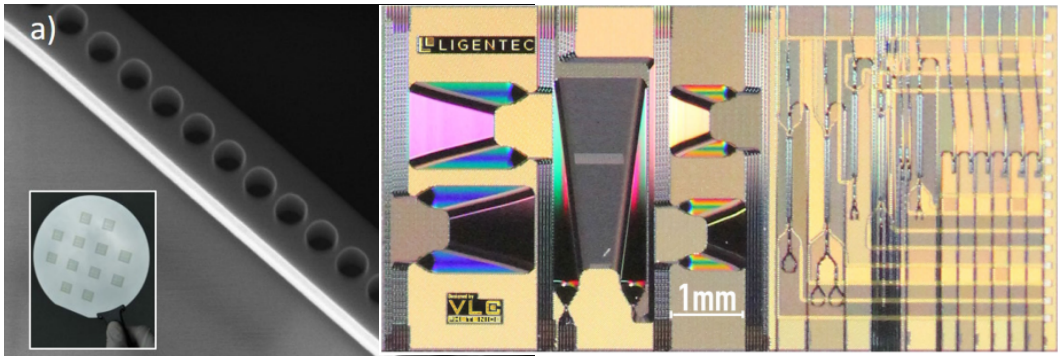

a) b)

Figure 1.5: a) AMO's Full Custom Silicon Photonic Rapid Prototyping Platform: Flexible process flows; High resolution photonic device layer (inset: finalized photonic wafer before dicing), [14]. b) Chip example from LIGENTEC consisting on five compact AWGs (left) and PDK building blocks with heaters for 1550 nm operation, [14].

Talking about the open-access SOI-based technology platforms offered here in Europe. We could highlight some foundries like Imec, which in collaboration with Ghent University, was among the first to demonstrate the power of deep ultra violet (DUV) lithography for silicon photonic ICs. CEA-Leti's, which has developed a fabrication platform for silicon photonics-based circuits allowing large-scale integration of active and passive devices in a flexible CMOS compatible process. IHP's monolithic electronic-photonic integration platform which is to deliver the integration of the basic components of electro-optic transceiver on a single chip. VTT's thick-SOI platform, which is based on 3 μm thick SOI where light is almost fully confined inside the Si core. AMO's silicon photonics platform, which provides a rapid prototyping silicon photonics platform for passive and active devices based on SOI substrates. And Cornerstone versatile wafer-scale which is a rapid prototyping multiproject wafer (MPW) capability that utilizes industrially-compatible tools, to enable seamless scaling-up of production volumes, whilst also retaining device level innovation capability using high-resolution lithography (e-beam) and versatile processes [14]. Here in Spain we could highlight nanophotonics technology center (NTC), located at the *Universitat Politècnica de València*, which offers also a rapid prototyping platform and is part of the *Red de Salas Blancas de Micro y Nanofabricación* together with the CNM (*Centro Nacional de Microelectrónica*) and the CT-ISOM (*Central de Tecnología del*

Instituto de Sistemas Opto-Electrónicos) in the framework of the *Infraestructuras Científicas y Tecnológicas Singulares* (ICTS) supported by the Spanish Government.

On the other hand, focusing in Si_3N_4 platforms we also have quite a few here in Europe. Starting for Ligentec, which has a process based on all-nitride-core technology and designed from the bottom-up for photonics and modularity. LioniX, which offers a platform with ultra-low loss, broad wavelength range of operation (400 - 2350) nm and the possibility to adapt the mode properties on the chip. Imec's, which started in 2012 with the development of a Si_3N_4 photonic platform with low losses in the visible and NIR range of the electromagnetic spectrum. AMO's, which has established a rapid prototyping Si_3N_4 platform offering passive devices and actives, which are based on thermo-optic effect. IMB-CNM, which is a moderate confinement Si_3N_4 photonics integration platform aiming at covering a wavelength range from (400 - 3700) nm for photonic integrated applications such as biophotonics, tele/datacom and sensing [14].

1.1.3 Space applications of PICs

The potential of photonics in space technology has been growing since the 1960s, when the only photonic devices on satellites were the solar cells. In recent years, photonic components and subsystems have become crucial for many functions onboard a spacecraft, e.g. for data processing attitude and orbit control, and load and thermal mapping. Currently many payloads for both Earth observation and scientific missions use a variety of optical and optoelectronic components, such as lasers detectors, modulators, lenses, gratings, etc. Although some photonic subsystems for the transport segment have been developed in recent years, most applications of photonics for the space segment have been carried out for the payload and the satellite platform. For some types of payloads, such as cameras and spectrometers, optical and photonic components have been used for several decades. While the use of photonic technologies in radar, telecommunication and navigation payloads is undoubtedly less, some technological demonstrators have already been developed [16].

Small satellites have become more attractive due to lower development costs and shorter lead times. Regardless of orbit and mission, there is a natural trade-off between satellite size and functionality in all current satellite applications. Still, advances in miniaturisation and integration technologies have reduced the extent of this trade-off. So, the use of photonic integrated circuits is quite interesting to achieve these kinds of requirements [17], [18]. In addition, as discussed in [19], satellite communication systems are increasingly looking to operate at higher frequencies in order to offer higher bandwidths and thus increase the data rate. So, photonics can play a crucial role in almost all satellite platform subsystems, compared to conventional technologies, because it is a suitable technology to operate at these frequencies.

Since first used in space in 1958, solar cells have been part of the power supply subsystem of all satellites. Some important advantages of fibre optics in implementing onboard data buses have been demonstrated on several space missions since the 1990s. Mapping strain and temperature in some critical areas of the spacecraft can benefit from the fibre Bragg grating technology, whose suitability for space has already been proven [16]. Finally, another aspect to highlight

is that optical wireless links can transmit data from one satellite to another satellite or from a satellite to a ground station, have successfully demonstrated space missions. In this latter case, the ground station is equipped with a suitable optical terminal containing many photonic components. This is one of the new applications of photonics in the ground segment. Some launchers are equipped with optoelectronic gyroscopes for attitude control guidance, while the fibre Bragg grating technology is very beneficial for monitoring the tanks in some launch vehicles.

RETINA project

In this section, we will describe the project on which this work is based, the RETINA programme, which is a consortium formed by *DAS Photonics S.L*, *Airbus Italia*, *AMO GmbH*, *STFC Rutherford Appleton Laboratory* and *Universitat Politècnica de València*. The RETINA project's main objective is to develop an advanced reconfigurable multibeam photonic beamformer with centralised processing. In particular, a very innovative synthetic aperture radar (SAR) an approach based on photonic technologies whose principal impact is to increase the EU competitiveness in payloads for advanced SAR missions by bringing to TRL 5-6 previous developments in photonic enabled payloads for SAR applications starting from the previous FP7 project GAIA [17], [18]. Therefore, one of the goals of the RETINA project is the optimisation of a PICs in silicon-nitride technology implementing designs of true-time delay (TTD) beamforming networks, suitable to be used in broadband applications without beam-squint degradation, implementing a frequency-agnostic switchable TTD beamforming matrix.

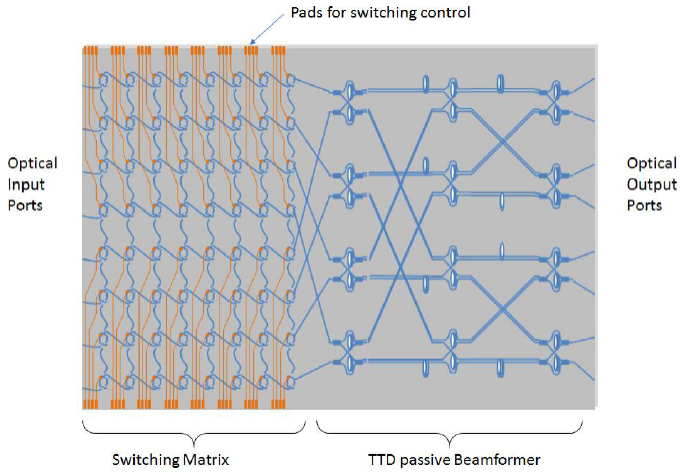

Figure 1.6: Elementary PIC-based 8x8 beamforming network [17], [18].

Optical beamforming

Within satellite communications, one of the most widely used applications is beamforming. And as reported in [20], photonics is one of the technologies able to satisfy several needs such as lightweight, immunity to electromagnetic interference and especially TTD, characteristics that current communication systems operating in the microwave band cannot achieve at the same level. To be more specific in the application, in this case, we intend to use optical beamforming for

a SAR, which usually operates in the C and X bands located in the so-called microwave spectrum. As indicated in [21], the requirements for this type of antenna are complex to implement with RF components, as several demanding thermal and mechanical requirements must be met. In addition, to meeting high bandwidths for today's new communication challenges. Therefore, photonics is increasing its presence in these types of systems.

According to [22], photonic beamforming in phased array antennas is an exciting example of the application of optical technology in wireless transmission systems. The motivation for phased array beamforming in the optical range depends heavily on the integration of beamforming functionality into optical chips. This leads to a great number of benefits mentioned before, such as small size, low weight, low losses, low production and installation costs, improved thermal and mechanical stability and inherent insensitivity to electromagnetic interference [23]. That leads to optical systems a clear advantage in these fields to implements their technologies.

In this case, the system consists of a group of multiple antenna elements (AEs), corresponding transmitting and receiving units, and a beamformer, which provides the direction-sensitive transmission and reception of electromagnetic waves. As it is reported in [21] usually the antenna photonic front-end systems are designed integrating the TTD PICs with electro-optical and optoelectronic transducers to create a modular, ultra-compact, repeatable, bidirectional TTD front-end for the antenna sub-arrays that form the antenna tile. In a final system, multiple antenna tiles will include the operational SAR antenna which can have a typical length of several metres.

As is reported in [18], the proposed optical beamforming network with TTD characteristics for this project is constructed by aggregating elementary 8x8 beamforming networks based on switching function PICs. This elementary 8x8 network photonic chip is shown in Fig. 1.6. This component can control the delay of up to eight signals simultaneously and route and combine them to a specific beamforming port. The 3D aggregation of this elementary unit builds the complete SAR beamformer, which can steer the beam in any direction within the detection limits. A simplified schematic of this 3D aggregation and the connection of the PICs to the antenna via optical fibres is shown in Figure 1.7.

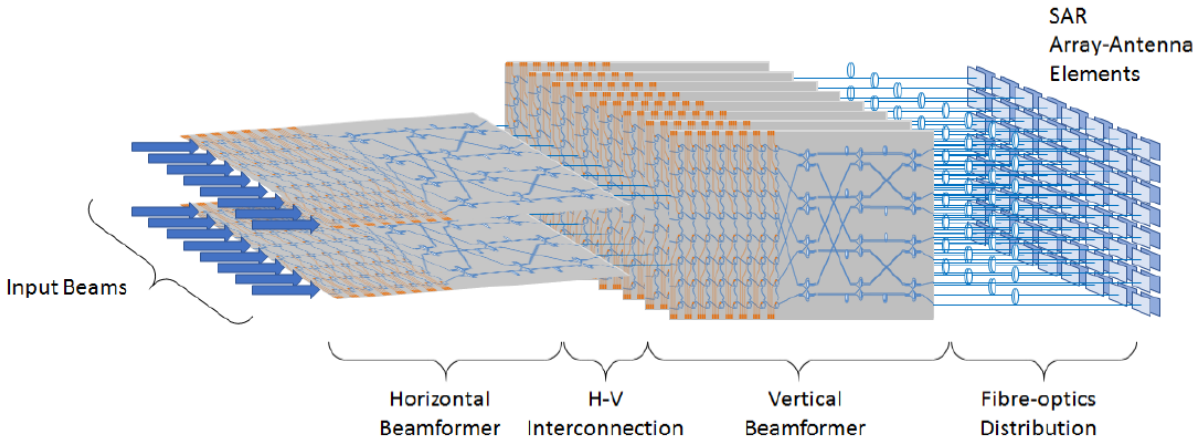

Figure 1.7: 3D aggregation of elementary 8x8 beamforming network PICs to construct the complete SAR beamformer [17], [18].

To meet the high technical requirements of the surrounding system, shallow insertion loss, Si_3N_4 technology is used for extremely low loss waveguides. The cross-section of the waveguide will be explained in next chapters, but basically the waveguide core consists of a silicon nitride waveguide with a width of 2.8 μm and a height of 100 nm, which lies on a 6 μm thick buffer layer of SiO_2 separating it from the silicon substrate. The waveguide core covers a 1.6 μm thick low-temperature oxide (LTO) (SiO_2 in this case) cladding layer. In addition, a metallic layer is deposited on the optical waveguide to implement micro heaters, which are required for the construction of thermo-optical switches.

1.2 Objectives

The main objective of this Master Thesis is to study and demonstrate ultra-low loss electro-optical switches manufactured in silicon nitride technology to operate in satellite applications in space. This analysis will focus on the design and composition of each part of the switch, explaining each critical aspect and the key factor in each case. In addition, an explanation of the design and manufacturing process of the integrated optical circuit will be provided to contextualise the task of this work. Finally, the experimental results of the characterisation of these devices will be presented and analysed, highlighting their most important parameters.

1.2.1 Document organisation

The report is organised into chapters, divided into sections and subsections. The organisation in terms of the content of the chapters is as follows:

- **Chapter 1: Introduction:** This chapter explains the motivation and the state of the art of the technology studied in this work. In addition, the project's objectives are described, as well as the time distribution of the work tasks.
- **Chapter 2: Switch design:** This chapter presents an explanation and description of the components that make up the complete thermo-optical switch system. In order to justify each step chosen in the design process, which has a decisive effect on the switch's performance.
- **Chapter 3: Switch characterisation:** This chapter describes the characterisation processes that have been carried out to test the behaviour of the switches.
- **Chapter 4: Conclusions and future work** Finally, this chapter sets out the conclusions drawn from the work and presents some possible future directions for further research.
- **Bibliography:** Lists the referenced works in order of appearance.

1.3 Methodology

1.3.1 Project development

A series of tasks described below had to be structured in five differentiated parts to carry out this work. The first has consisted of collecting and interpreting bibliographical material, which was used to develop part of Chapter 1 to show the motivation for this study and review the state of the art. This has also enhanced explanations in chapter 2 to understand the device's operation and many parts of its design.

In the second part of this work the design and simulation of most components that make up the switch have been carried out in order to improve their design parameters and to check that the expected results are obtained. Then, in the third part, we proceeded to carry out the experimental part of the project. In each case, we prepared the necessary setups for each type of experiment and proceeded to carry out the appropriate measurements to test the performance of the devices of interest.

Finally, the fourth part has consisted of carrying out all the processing of the data obtained, both in terms of simulations and characterisation. In order to be able to represent and evaluate them clearly and effectively. Finally, the last part of this work has based on writing this document in which all the work is presented, and the results and conclusions are obtained.

1.3.2 Task distribution

1. **Review literature**
   (a) Photonic integrated circuits
      - Silicon on insulator state of art
      - Silicon nitride state of art
   (b) Switching parameters and mechanism
   (c) Photonic components design
2. **Design and simulations with commercial simulator R-soft**
   (a) Design of used waveguides
      - Calculation of TE and TM main modes
      - Study of dispersion in both polarisations
   (b) Design of MMIs
      - Calculation of TE and TM main modes
      - Study of dispersion in both polarisations
   (c) Design of optimum active length
   (d) Design of heaters performance

3. **Experimental characterisation of the devices to be studied**
   (a) Static characterisation
   (b) Temporal characterisation
4. **Analysis and processing of the data obtained both in the simulations and characterisation**
   (a) Develop the scripts to read and manage all the data useful for the evaluation of the devices
   (b) Elaborate graphics to show clearly all results obtained.
5. **Writing the report**
   (a) To set out as clearly as possible all the work carried out

1.3.3 Time diagram

Finally, the above tasks can be organised in a time diagram to show how they have been planned over time:

Task	January			February			March			April			May			June	
1	X	X	X	X													
2			X	X	X	X											
3					X	X	X										
4						X	X	X	X	X							
5										X	X	X	X	X	X	X	X

Table 1.1: Time diagram of tasks.

Chapter 2

Switch design

This section addresses the design of the switch. The structures that comprise the switching device are described in order to justify the usefulness of each of them, highlighting the main characteristics that encourage their choice for the functions expected of them.

2.1 Si_3N_4 photonic waveguide

Starting with the type of waveguides chosen for this design, it is necessary to talk first about the type of technology selected for this purpose. Depending on the intention of application of these circuits, a kind of technology is better than the other. In the case of this project, all components have been implemented in silicon nitride. This technology offers ultra-low losses due to lower mode confinement in the waveguide compared to silicon. Minimising the optical losses is crucial when developing this satellite application.

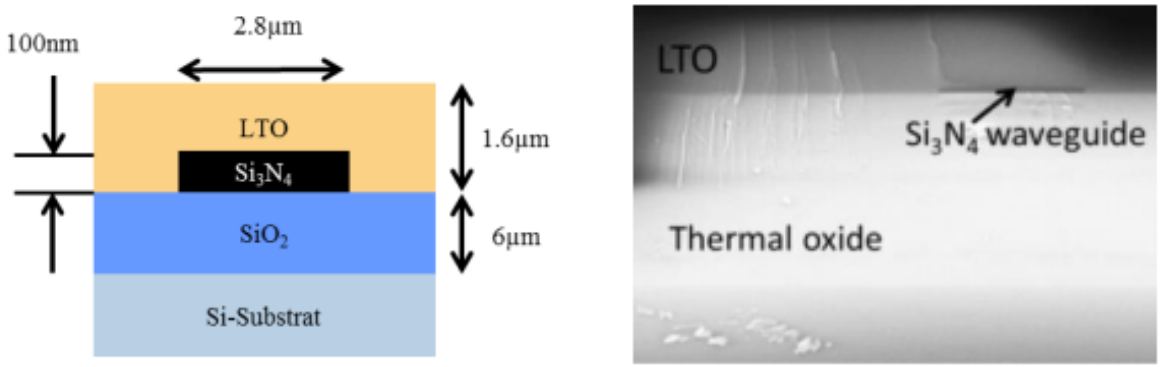

a) b)

Figure 2.1: a) Ultra-low loss photonic waveguide cross-section. b) Micrograph of fabricated waveguide. [17]

As is mentioned in [24], the proposed platform shown in Fig. 2.1 a) is based on the ultra-low

loss Si_3N_4 photonic waveguide. The core consists of a 100 nm thick and 2.8 μm wide silicon nitride waveguide, located on top of a 6 μm thick silicon dioxide buffer layer that separates it from the silicon substrate. In addition, the waveguide core is covered by a 1.6 μm thick LTO cladding layer. The design is optimised for transverse electric polarisation (TE), but the orthogonal, transverse magnetic polarisation (TM) also it will be studied.

2.1.1 Simulation of waveguide modes

The optical modes of the Si_3N_4 and Si waveguides have been simulated in RSoft software using the FemSim tool. In order to compare these technologies the Si_3N_4 waveguide with the dimensions specified in Fig. 2.1 a) (2800x100) nm has been considered against a silicon waveguide with its typical dimensions (500x220) nm. The result shown in Fig. 2.2 is as follows.

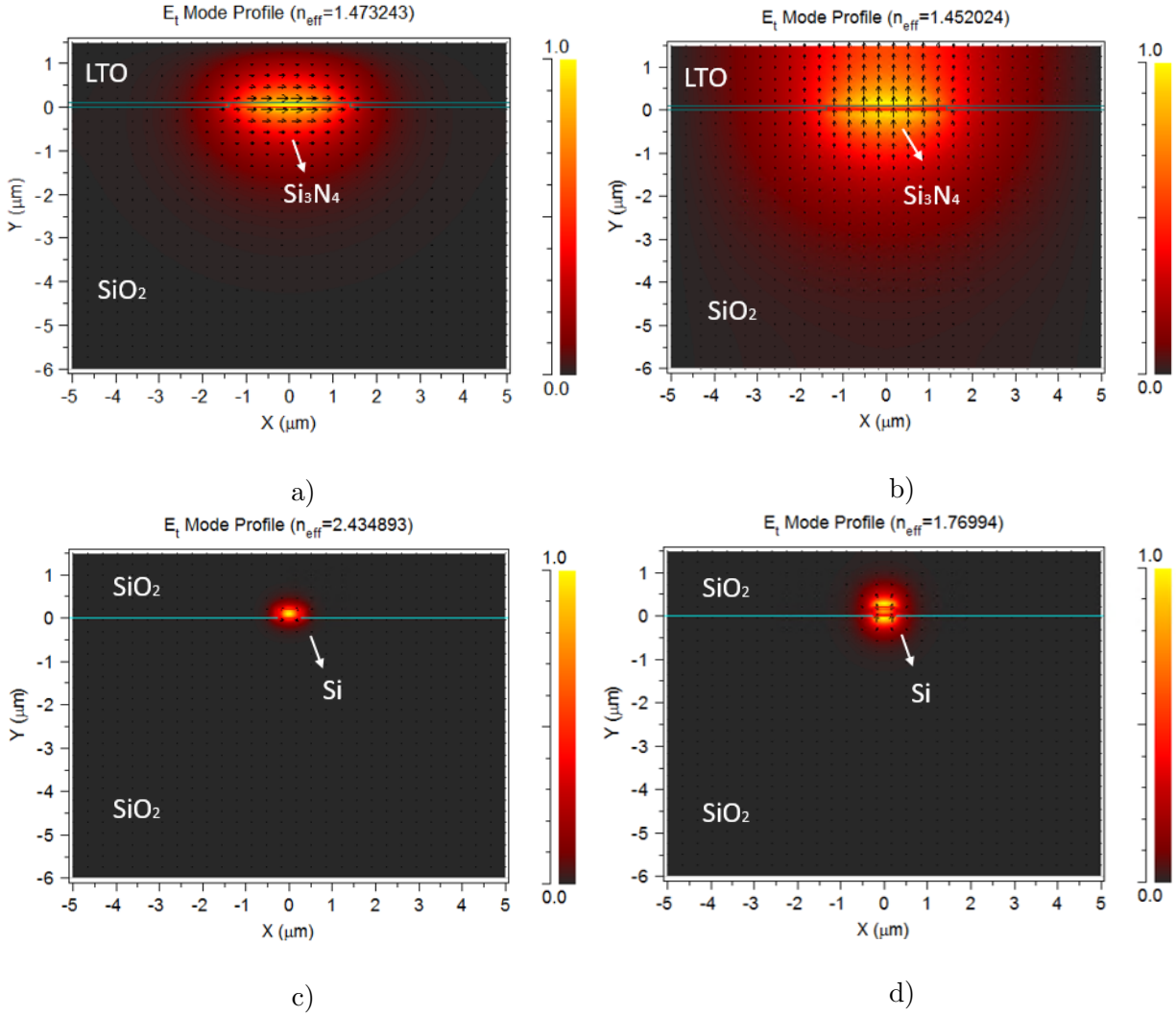

Figure 2.2: a) TE mode of Si_3N_4 waveguide. b) TM mode of Si_3N_4 waveguide simulated in FemSim tool. c) TE mode of Si waveguide simulated in FemSim tool. d) TM mode of Si waveguide. All the results are simulated in FemSim tool and are given at $\lambda = 1550$ nm.

As can be seen, due to the lower Si_3N_4 index, the mode confinement in the waveguide is

lower than in the case where silicon technology is used. Therefore, it can be deduced that by having a less confined mode, propagation on Si_3N_4 suffers less from losses due to roughness on the waveguide walls. This was one of the main reasons this technology was chosen to develop the devices for this project. As mentioned before, minimising waveguide losses was a key factor for this application.

It should be noted that in telecommunications, the behaviour of the components varies according to frequency. The same is valid for wavelength in photonics, as the bandwidth of many components, e.g. MZIs, MMIs, directional couplers, etc., depends on their n_{eff}, which is a wavelength function. Thereby, the dispersion of the waveguides has also been simulated for each mode, i.e. it has been calculated how the effective index varies as a function of wavelength. In this way, it is possible to check which technology has the best bandwidth performance.

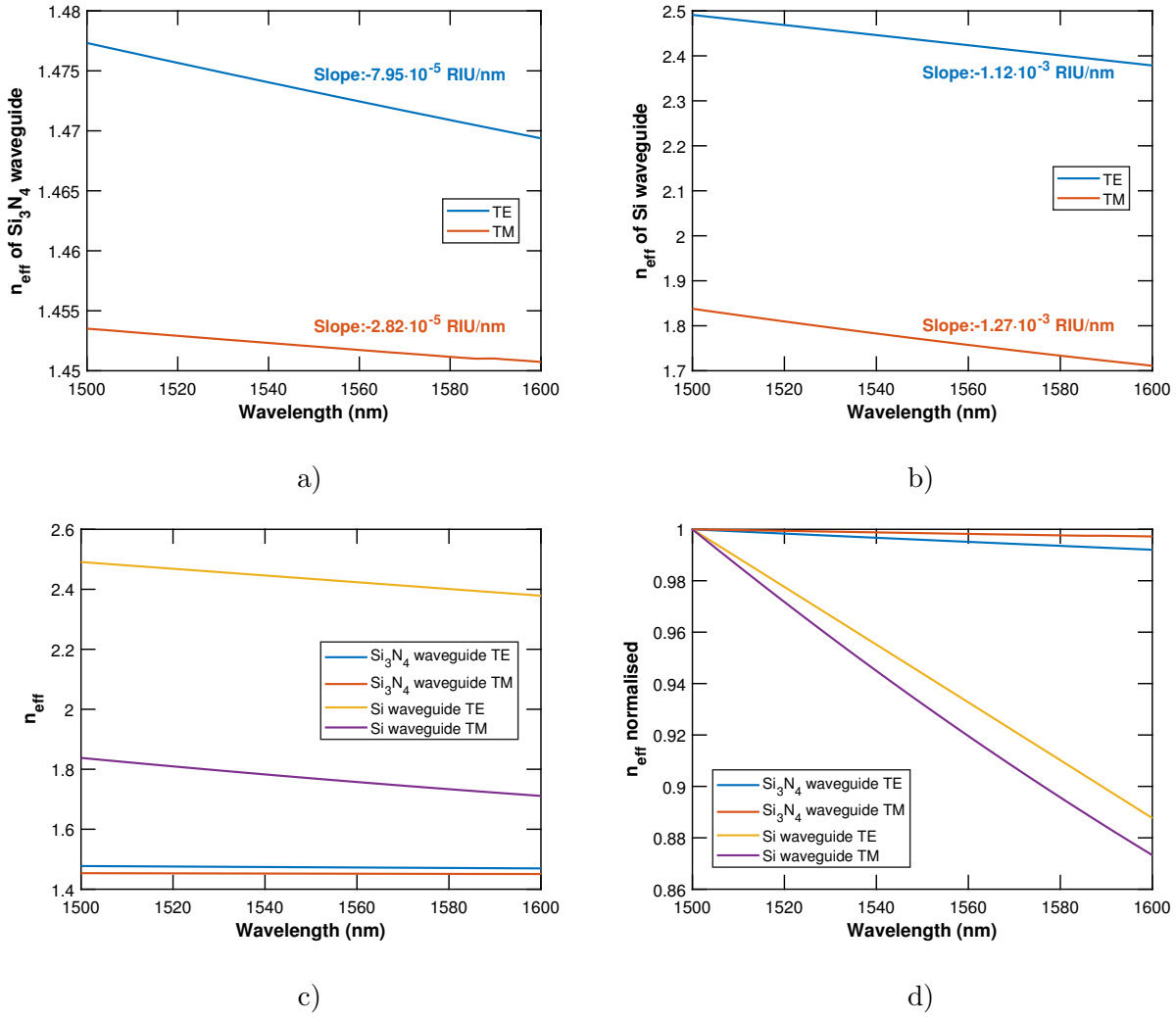

Figure 2.3: a) Comparison between TE and TM modes dispersion in a Si_3N_4 waveguide. b) Comparison between TE and TM modes dispersion in a Si waveguide c) Comparison of the dispersion between Si_3N_4 and Si waveguides. Both in TE and TM. d) Comparison of the dispersion normalised between Si_3N_4 and Si waveguides. In order to compare all results in the same graph. Both in TE and TM.

As can be seen in Fig. 2.3 a) and b), it appears that the silicon waveguide is more dispersive,

for both TE and TM. Since the slope of its n_{eff} lines (both in TE and TM) is two orders of magnitude higher than the Si_3N_4 waveguide. Finally, comparing all the results in the same graph, especially in Fig. 2.3 d), where the n_{eff} values are normalised to one, so that the results can be compared with the same axes. It is confirmed that the modes through the silicon waveguides suffer more scattering, as they have a steeper slope than Si_3N_4 ones. It follows that the Si waveguide has significantly lower bandwidth performance and a higher dependence on the $V\pi$ and $P\pi$ values in the switch. This implies that it should have more complex electronics and, therefore, higher costs.

2.2 Choice of switch

The main components of this project, the switches based on a Mach-Zehnder interferometer (MZI), 2x2 structure, will be explained in this section to show their principles of operation.

Therefore, this section will explain what an electro-optical switch consists of and what the physical mechanisms are for achieving commutation in photonic systems. In addition, a breakdown of the basic elements that make up a switch will be given, and the relevance of each component within the overall system will be explained in detail.

2.2.1 Theory about optical switches

Optical switches are one of the essential building blocks of optical networks. In addition, these devices allow switching directly in all optical domains, avoiding the need for several conversions between optical and electrical domains. For these reasons, various physical modulation mechanisms are based on achieving the index change of the material of the technology in question, in this case, silicon nitride, to accomplish this change in the signal. These effects can be thermo-optical, electro-optical among others.

Switching/modulation mechanisms

One significant effect is the electro-optical effect, which, according to [25], is a change in the optical properties of a material in response to an electric field that changes slowly compared to the frequency of light. On the other hand, we could highlight the plasma scattering effect, which changes the concentration of free charge carriers, leading to changes in semiconductor materials' refractive indices and absorption coefficients [26]. However, we do not explain these effects much since they are not the physical principle of the application studied in this work.

Therefore, it remains to explain in this section the thermo-optic effect, which is the basis of the switches that will be studied in this work. As reported in [27] the thermo-optic effect is a well-known phenomenon in physics. It determines the change in the refractive index with a temperature variation. This effect is used in optoelectronics and sensor technology for the realisation of a multitude of devices, which are mainly based on interferometric principles, such

as optical switches, tunable filters, tunable lasers and fibre optic sensors and others. According to [28] the thermo-optic effect has probably the highest potential in component-level simplicity and application perspectives, constituting a well-conceived and more mature approach. Furthermore, tuning through the thermo-optic effect presents the advantages of a large refractive-index tuning range and negligible optical loss compared to electro-optic tuning [29]. That is why it is so attractive for the application of this work.

The thermo-optic effect is a change of the refractive index with temperature, where the variation of both variables follows a linear relationship between them. This means that the increase in temperature leads to an increase in the effective index of the mode. According to [30] the thermo-optic coefficient of Si_3N_4 is:

$$\frac{dn_{Si_3N_4}}{dT} = (2.45 \pm 0.09) \times 10^{-5} \ \ (\mathrm{RIU}/^{\circ}\mathrm{C}) \tag{2.1}$$

Switching/modulation parameters

Furthermore, as modulation and switching are closely related concepts, the most important parameters used to characterise the performance of modulation and switching will be explained in order to lay the groundwork for the subsequent analysis to be carried out in this work. According to [26] they would be:

The extinction ratio (ER), which is the ratio of the output power in the on-state of the switch to the output power in the off-state. This ratio should be as large as possible. In telecommunications, the ER is the ratio of two, the optical power level of a signal transmitted from an optical source, e.g. a laser diode, where P_1 is the maximum optical power level generated, and P_2 is the minimum power level caused by the light source [ER = P_1/P_2]. As the next equation shown, the ER can be expressed in linear units or in dB. The measurement of the ER can also be carried out using an eye diagram also.

$$ER = 10\log(\frac{P_{max}}{P_{min}}) \tag{2.2}$$

Also it is important to know insertion loss (IL), this is defined as the optical losses induced by the switch when it is in the ”on” state. These losses are usually measured in decibels and must be as low as possible. Furthermore, the IL of a switch should be nearly the same for all input-output connections. In other words, IL are the total losses of the entire switch, including the coupling losses, the propagation losses in the waveguide, and the absorption losses in the modulation region. If the input power and output power are P_{in} and P_{out}, respectively, its IL can be written as:

$$IL = 10\log(\frac{P_{in}}{P_{out}}) \tag{2.3}$$

Another important parameter is switching time, which imposing a square-wave signal in

the switch, the output is also a square-wave signal. The difference between the maximum and minimum output power is defined as:

$$\Delta P = \mathrm{P}_{max} - \mathrm{P}_{min} \tag{2.4}$$

For this purpose, the concepts of the rise time t_r and fall time t_f are defined. The former is the time experienced by the output power to increase from P_{min} + 10%ΔP to P_{in} + 90 %ΔP. Similarly, the latter is the time experienced by the output power to decrease from P_{max} - 10% ΔP to P_{max} - 90% ΔP. Hence, the switching time, t_s, of a modulator is the larger value of rise time or fall time. In line with this, it would be highlighted the modulation bandwidth which can be defined as the modulation frequency while the ER reduces to half of the maximum. It is often associated to the switching time t_s:

$$f_{3dB} = \frac{0.35}{\mathrm{t}_s} \tag{2.5}$$

In accordance with the parameters of the switches, we should also talk about crosstalk CT, which refers to any phenomenon by which a signal transmitted on one circuit or channel of a transmission system produces an undesirable effect in another circuit or channel. Crosstalk is usually caused by unwanted coupling from one circuit, part of a circuit or channel to another. This is the ratio of the power at a particular output and it is defined as follows:

$$CT = 10\log(\frac{P_{out_n}}{P_{in}}) \tag{2.6}$$

2.2.2 Optical switch structure

The switch configurations considered are based on Mach-Zehnder interferometer (MZI) and multimode interference (MMI) designs. Therefore, an overview of these devices' theoretical behaviour will be given to understand their role within the switch system.

MZI structure

As is described in [1], the Mach-Zehnder interferometer is based on the interference between two optical signals coming from the exact origin and travelling along the different effective lengths. This extra effective length creates a phase difference converted into a change in output power as the two signals are combined at the end. The phase difference, therefore the MZI response, depends on the wavelength, and polarization of the input signal and it can be represented as:

$$\Delta\phi = \beta_2 L_2 - \beta_1 L_1 \tag{2.7}$$

As can be seen, this difference in effective length can be generated in several ways. On the one hand, one can play with the physical length difference between the two arms of the MZI. But on the other hand, it can also be achieved by varying the β, which, as it is well known, is $\beta = 2\pi n_{eff}/\lambda$. So, changing the n_{eff} is also possible to achieve this desired phase shift. Fig. 2.4 shows a clear example of the first case, where this difference in distance between the two branches occurs.

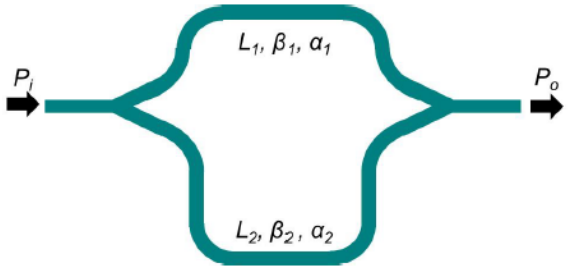

Figure 2.4: MZI 1x1 with an asymmetric structure, [31].

$$\Delta\phi = \beta(L_2 - L_1) \tag{2.8}$$

As it can be seen in the Fig. 2.4, an MZI consists of an input split into two branches and then brought together again. The splitting or combining can be done with any splitter combiner, including Y-branches, MMIs and directional couplers among others. Following [1] explication, at the output of the first Y-branch the top branch would have field $E_1 = E_i/\sqrt{2}$ and the bottom branch has $E_2 = E_i/\sqrt{2}$. The propagation of light in the waveguides is described by $\beta_1 = 2\pi n_1/\lambda$ and $\beta_2 = 2\pi n_2/\lambda$, and propagation loss α_1 and α_2, and the waveguides have lengths L_1 and $L_2 = L_1 + \Delta L$. In this case, the electric field equations in an MZI are described in general terms. As seen in them, the phase difference between each branch can be marked by the difference in lengths as explained in Fig. 2.4 and in n_{eff} as shown in Fig. 2.5.

$$E_{o1} = E_1 e^{-i\beta_1 L_1 - \frac{\alpha_1}{2}L_1} = \frac{E_i}{\sqrt{2}} e^{-i\beta_1 L_1 - \frac{\alpha_1}{2}L_1} \tag{2.9}$$

$$E_{o2} = E_2 e^{-i\beta_2 L_2 - \frac{\alpha_2}{2}L_2} = \frac{E_i}{\sqrt{2}} e^{-i\beta_2 L_2 - \frac{\alpha_2}{2}L_2} \tag{2.10}$$

The field at the output of the MZI, which would correspond to the field at the output of the Y-branch combiner, would be:

$$E_o = \frac{E_i}{2}\left(e^{-i\beta_1 L_1 - \frac{\alpha_1}{2}L_1} + e^{-i\beta_2 L_2 - \frac{\alpha_2}{2}L_2}\right) \tag{2.11}$$

Once the output field value has been defined, the free spectral range FSR can also be calculated, which determines the separation between the resonances caused by the interferometric

structure, in this case, the MZI. This FSR value is defined in both the frequency and wavelength domains as follows:

$$FSR\ [\text{Hz}] = \frac{c}{n_g \Delta L} \tag{2.12}$$

$$FSR\ [\text{m}] = \frac{\lambda^2}{n_g \Delta L} \tag{2.13}$$

where c is the speed of light in vacuum, and n_g is the waveguide group index while ΔL is the difference in paths between the two arms of the MZI. It can therefore be seen how the physical parameters of the device design affect its final performance, in this case by marking the distance between the resonances.

As mentioned above, there are two ways to achieve the offset between the two signals crossing the MZI. The difference in distances between the two paths which has already been discussed above. Therefore, here in Fig. 2.5, we show the other one, which is just a change in the effective material index, keeping the length of each branch constant. For this, any physical effects, whether electro-optical or thermo-optical, described earlier in this work, are used. Obviously, this document will focus mainly on the thermo-optic effect to switch.

$$\Delta\phi = (n_{eff1} - n_{eff2}) \frac{2\pi}{\lambda} L \tag{2.14}$$

a) b)

Figure 2.5: a) MZI 1x1 with symmetric structure, [31]. b) Active performance in order to change n_{eff}, [31].

Finally, it should be noted that having seen the two methods of achieving switching in MZIs, it must be said that in the world of integrated photonics, the second method, i.e. that of phase shift based on the change in the signal index, is usually more common. This is because, in this way, with the same MZI design, the response of the MZI can be actively controlled without having to modify and remanufacture the design with the economic overhead that this entails. In addition, as both branches of the device have the same size, it is also easier to make the most of and optimise the space on the chip where it is integrated, which is another critical parameter that has to be taken into account.

MZI to switch

Having seen the theory of the main component of this system, which is the MZI, we will now look at how to build the switch from this first component. To achieve this, a 2x2 MZI configuration would be needed, as shown in Fig. 2.6 a), which, as can be seen, would consist of two MMI couplers, one at the input and one at the output, together with the MZI structure.

According to [28], the principle of operation is as follows; First of all, an incident optical wave in one input of the 3 dB input coupler is equally divided between the two outputs feeding the MZI branches. If the propagation along the MZI branches is result in a relative phase shift of zero, then the switch is in the CROSS state, i.e. the light is recombining at the output of the 3 dB output coupler, which is opposite to the component input connector. Conversely, if the signal propagation through both arms achieves an offset of π, the switch is said to be in the BAR state. It implies that the output port would be on the same side as the input port.

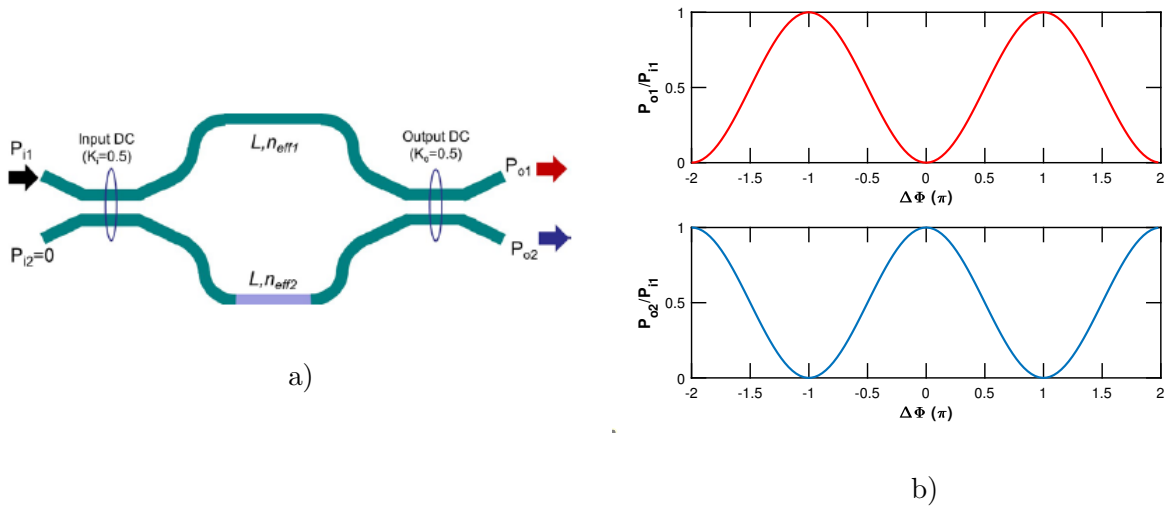

Figure 2.6: a) MZI 2x2 with symmetric structure, [31]. b) Theoretical response of each output of the switch, for input 1 of the device, in the CROSS state (without power supply).

The switching is achieved by controlling the refractive index of the addressable MZI branch, which in turn contains the phase shift between the two arms. The critical specification of a 2x2 switch, apart from its IL, is the ER value of the output port achieved in the CROSS and BAR states. This document defines the ER as the ratio of the conducted power between the two outputs when only one input is fed. For balanced switches such as this MZI (see Fig. 2.6 a)), both the input/output ports and the switching states are equally important. Consequently, we need to define an aggregate ER to characterise the component's performance without reference to a heated/unheated or BAR/CROSS state. This aggregate value is usually equal to the lowest, worst case, of the two states, corresponding to the minimum ER value in one of these states.

So it is clear that we need to estimate the ER in our switch, in any case, to design it properly. Following the description in [28], the most critical parameter of the MZI switch is the arm length required to achieve a π phase shift by the thermo-optical efficiency, which is quantified by the change in Δn. This index change, is considered to be uniform across the transverse cross-section

and is equal to the temperature shift ΔT times the thermo-optic coefficient of the material, as shows:

$$\Delta n = \Delta T \frac{dn_{Si_3N_4}}{dT} \tag{2.15}$$

Intuitively, a trade-off can be made between the component length and the temperature shift used, as the active part of the system could be burnt. However, it also should be borne in mind that longer arms are associated with higher IL. In a simple analysis of the transmission matrix and assuming ideal 3 dB couplers show that when both MZI arms are not heated, the 2x2 switch is in the CROSS state, regardless of the arm length. The characteristic length L_π for π phase shift in the heated temperature state, which corresponds to the BAR switch state, is given by

$$L_\pi = \frac{\lambda_0/2}{|n_{eff(U)} - n_{eff(H)}|} \tag{2.16}$$

where $n_{eff(U)} - n_{eff(H)} = \Delta_{eff}^{U-H}$ is the effective index difference between the unheated "U" and heated "H" states. Therefore, we would have a formula from which we would only need to know the operation wavelength and effective modes when it is in its natural state (CROSS state) and then when it is heated (BAR state).

2.3 Design of optical elements

Having explained the basics of the MZIs, which are the main component of the switches, we will now explain and justify the other elements, such as the MMIs, as they also play an essential role in the overall switch system.

2.3.1 MMI couplers

A multimode interference coupler MMI is a structure with N input ports and M output ports connected to a multimode waveguide, which can support a large number of guided modes. The working principles are based on the self-imaging effect, which consists mainly of periodically repeating the input excitation in one or multiple images along the propagation direction, as shown in Fig. 3. As it is cited in [32] the self-imaging effect could be described as a property of multimode waveguides by which an input field profile is reproduced in single or multiple images at periodic intervals along the propagation direction of the waveguide.

The central structure of an MMI device is a waveguide which is designed to support a large number of modes (typically ≥ 3). In order to couple light into this multimode waveguide and radiate it in and out of this one, a series of access waveguides is used at the beginning and end of the access waveguide. Such devices are generally called NxM MMI couplers (see Fig. 2.7), where N and M are the number of input and output waveguides, respectively.

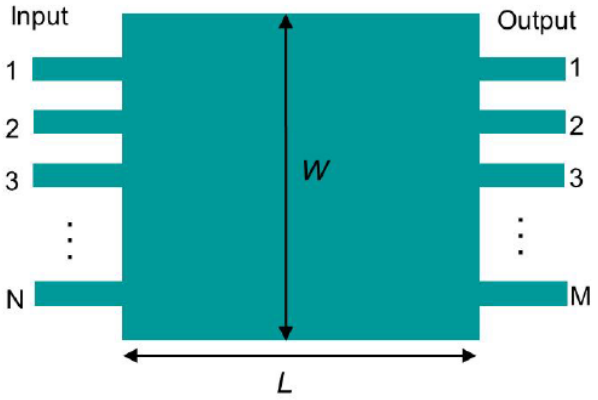

Figure 2.7: MMI structure NxM, [31].

Given the design of the switch being studied in this work, the MMI should have an NxN configuration (i.e. the same ports at the input as at the output), in this case, two. On the other hand, we are also looking for the output to have the same power on each arm of the device, i.e. a 3-dB coupler.

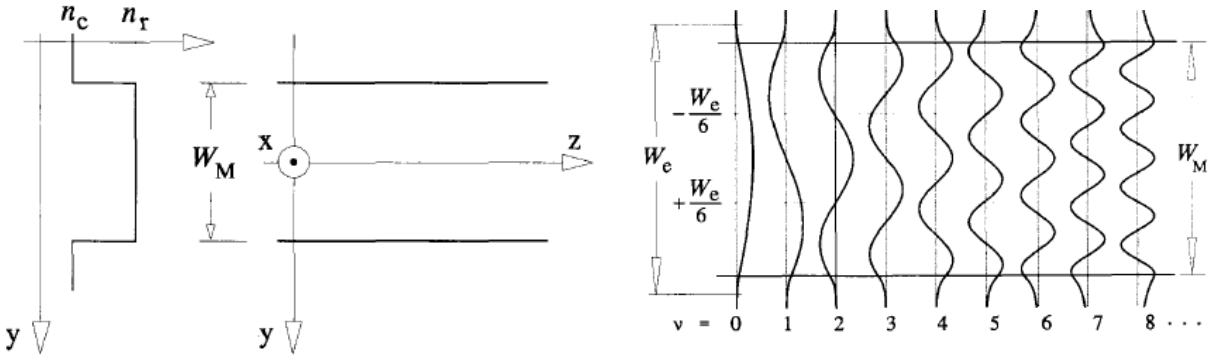

a) b)

Figure 2.8: a) Two-dimensional representation of a step-index multimode waveguide, [32]. b) Example of amplitude-normalized lateral field profiles corresponding to the first 9 guided modes in a step-Index multimode waveguide, [32].

To do this, we always start by choosing the width W_M of the MMI multi-mode waveguide, which, the narrower, the better, because as it is a structure that is going to be integrated, saving space is a priority. However, it should also be considered that if too small W is chosen, there will be too little separation between the MMI ports, leading to a possible unwanted coupling between them. Therefore, there must be a trade-off between W_M and the spacing between ports, although in this case, as the device is a two-arm MMI, this will not be such a critical parameter.

Once W_M is chosen, the next step is to obtain the length L of that guideway, which in this case, where there is the same number of incoming and outgoing ports, could be calculated as follows:

$$L_{NxN} = \frac{3L_\pi}{N} \tag{2.17}$$

where N is the number of ports. It can be seen that the result depends on a parameter called the beat length L_π , which there are different methods to calculate. On the one hand, one could create a waveguide with the width W chosen at the beginning and simulate its modes in a commercial simulator such as FemSim, and from this expression:

$$L_\pi = \frac{\lambda}{2|n_{eff0} - n_{eff1}|} \tag{2.18}$$

obtain its value, knowing that n_{eff0} and n_{eff1} refer to the fundamental and first-order modes which are shown in Fig 2.9.

On the other hand, according to L.B. Soldano in [32], this L_π could also be obtained from the expression

$$L_\pi = \frac{4n_r W_{eff}^2}{3\lambda} \tag{2.19}$$

It is known that n_r refers to the refractive index of the waveguide and n_{cd} to the cladding index. On the other hand, the W_{eff} refers to the lateral penetration depth of each modal field, which is dependent with polarisation and assuming a number of approximations, can be calculated as:

$$W_{eff} = W_M + \frac{\lambda}{\pi}\left(\frac{n_{cd}}{n_r}\right)^{2\sigma}\left(n_r^2 - n_{cd}^2\right)^{-1/2} \tag{2.20}$$

where σ is the value that marks this polarisation dependence, being $\sigma = 0$ for TE and $\sigma = 1$ for TM.

Taking into account the values used for the actual design of this device as explained in [33], such as that the MMI must be 2x2, and also knowing the width of the silicon nitride waveguides $W_{Si_3N_4} = 2.8$ μm, a value of $W_M = 10.5$ μm has been chosen for the width of the multimode waveguide, leaving a distance between ports of $d_{MMIports} = 4.9$ μm. Therefore, doing the relevant calculations would give the results shown in the following table, which shows the final result of the MMI length using both methods for the two polarisations. As can be seen, the best result (shortest multi-mode waveguide) is obtained with the first method for TE. It is also the closest to the actual value chosen for the design, $L_{MMI} = 238.8$ μm. In this case, both the fundamental and first-order TE and TM modes of the Si_3N_4 waveguides have been compared in Fig. 2.9.

First method (Eq. 2.18)		**Second method (Eq. 2.19)**	
TE	**TM**	**TE**	**TM**
252.55 μm	298.31 μm	288.35 μm	279.55 μm

Table 2.1: Calculation of the MMI lengths for both polarisations, using the two methods explained.

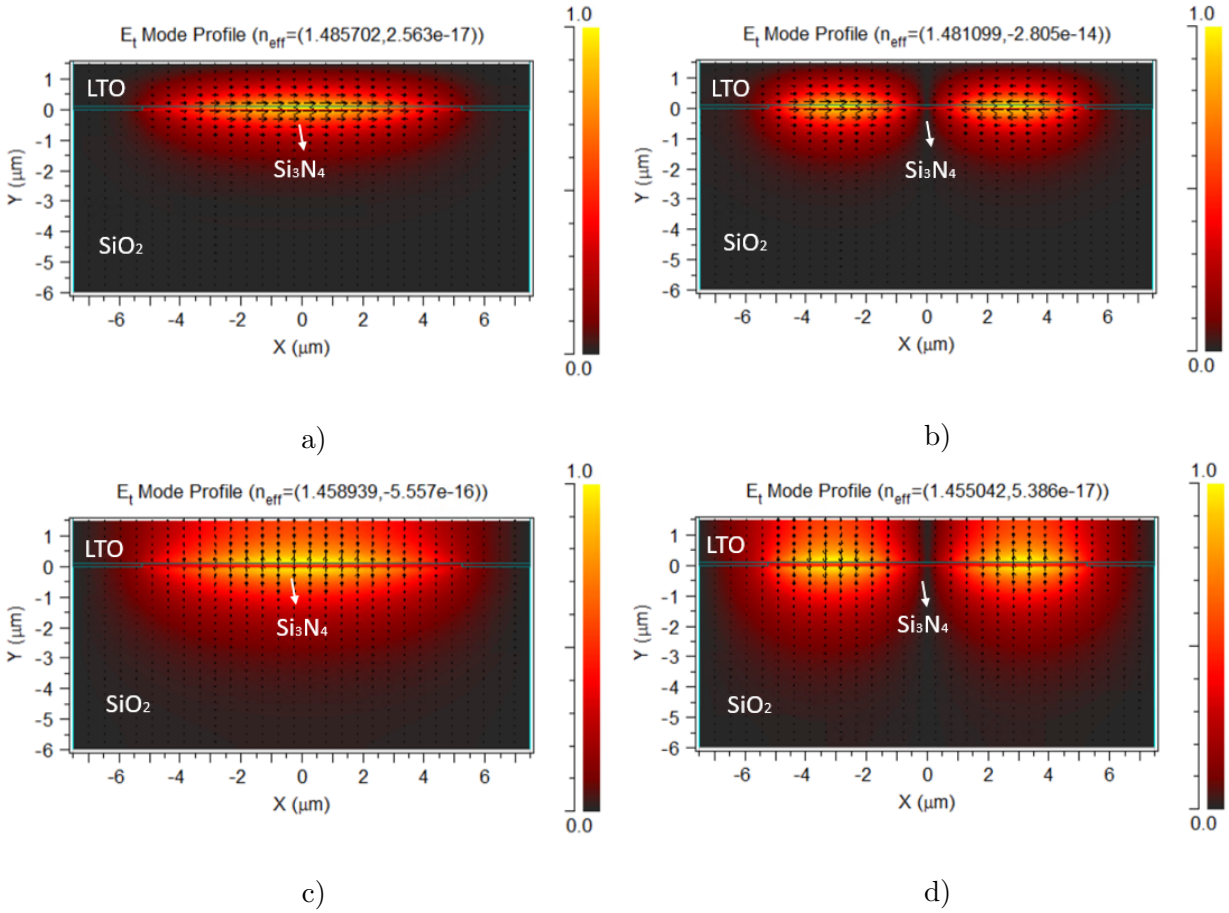

Figure 2.9: a) Fundamental TE mode multi-mode Si_3N_4 waveguide. b) First-order TE mode multi-mode Si_3N_4 waveguide. c) Fundamental TM mode multi-mode Si_3N_4 waveguide. d) First-order TM mode multi-mode Si_3N_4 waveguide. All the results are given at $\lambda = 1550$ nm.

Rationale for MMI couplers

The following is intended to indicate/justify the reason for the choice of MMI devices. Whatever input is chosen for injecting the signal, the output always has the same power on both ports, as if it were a 3-dB directional coupler. It should be known if other devices could fulfil this function. However, the MMI also offers broadband performance and low polarization dependence, this makes it the perfect aspirant for applications where it is necessary to cover a considerable bandwidth, such as the SAR system to be developed. In addition, it could be highlighted its high tolerance to fabrication deviations makes this device the best candidate for this application.

As previously done, to also demonstrate the better bandwidth performance of Si_3N_4 compared to silicon technology. The wavelength dispersion of the first fundamental and first-order modes TE and TM (see Fig. 2.9) of Si_3N_4 multimode waveguide will be plotted to demonstrate the great performance in bandwidth of this technology also in a multimode waveguide.

As shown in Fig. 2.10, it appears that the type of TE or TM polarisation does not affect much to the dispersion. Since the slope values in all cases are in the same orders of magnitude. However, comparing all the results with the same reference axis (Fig. 2.10 b)) shows that the

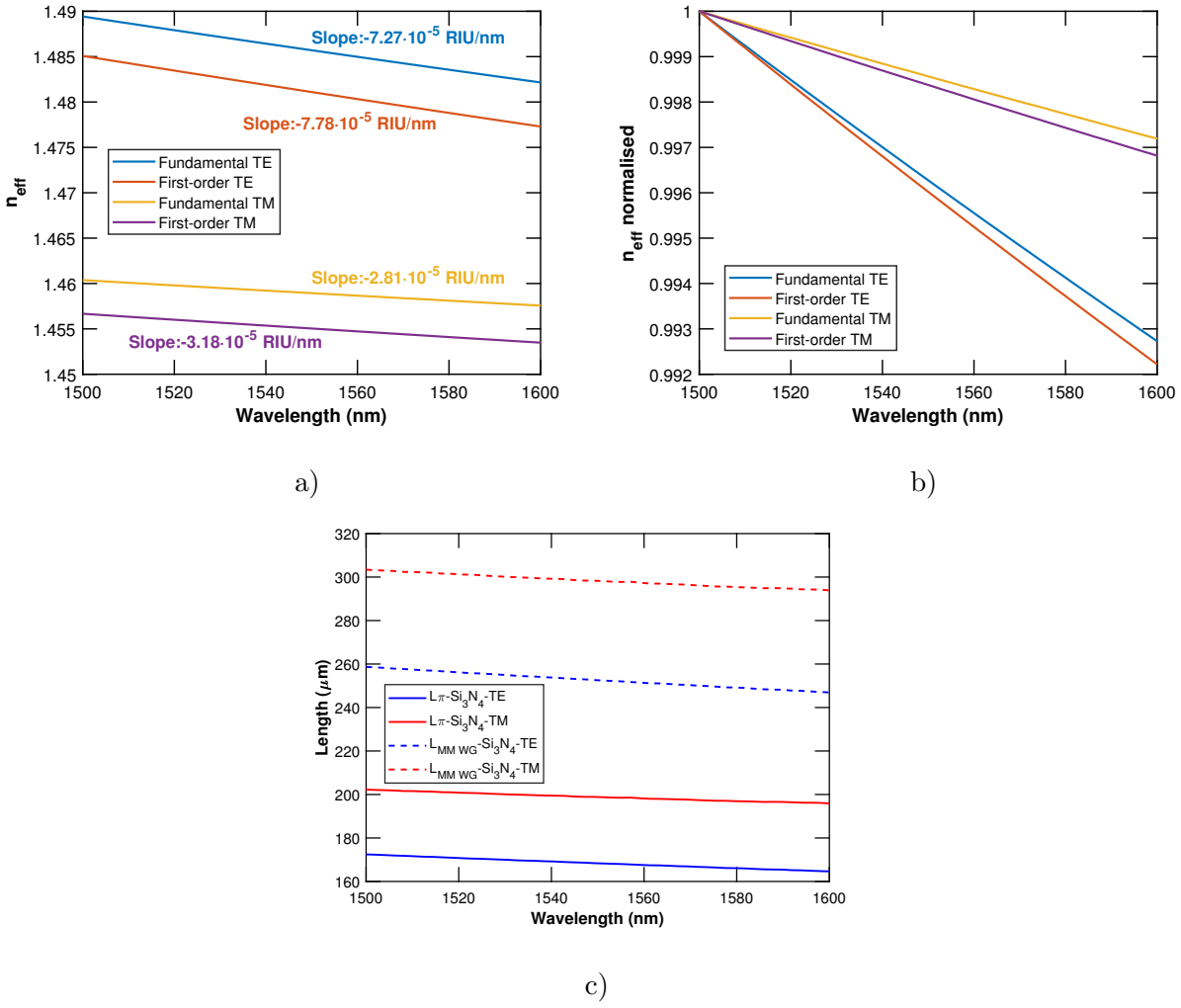

a) b)

c)

Figure 2.10: a) Comparison of the dispersion in a Si_3N_4 waveguide between even and odd TE and TM modes. b) Normalised comparison of the dispersion in a Si_3N_4 waveguide between even and odd TE and TM modes. In order to compare all results in the same graph. c) Beat length L_π and multimode waveguide length, of a Si_3N_4 waveguide for first TE and TM modes.

TE modes are slightly more dispersive than TM modes, but with little significant difference. Then, the beat length L_π, and the multimode waveguide length, have also been obtained from the fundamental and first-order TE and TM modes in this spectrum. Using for this purpose Eq. 2.17 and 2.18 respectively. Looking at Fig. 2.10 c), both lengths in TE and TM do not vary much as a function of wavelength. Nevertheless, larger length values are needed for TM, so it follows that more compact designs are achieved for TE.

MMI couplers simulation

To test the performance of these MMIs, the commercial simulator BeamProp integrated into the Synopsis RSoft package has been used. As is described in [34], this simulator is a very efficient tool for fiber and waveguide devices. It is based on beam propagation method (BPM), which solves Maxwell's equations by making assumptions such as not considering time data,

i.e. it is in a steady-state. Furthermore, only one wavelength can be simulated at a time, so it is a monochromatic tool. Finally, it is designed for structures where light must travel in one direction, valid for most waveguide and fiber devices. The performance of an MMI is based on the coupling between multiple modes over its length. This coupling is determined by the difference of the modal effective indices [35]. BPM is an efficient algorithm for photonics with reasonable accuracy. Although BPM has its limitations, such as backward reflection from abruptly varying structures, it is a suitable approach for fast prototyping, being 1000 times faster than the finite-difference time-domain method (FDTD), one of the most algorithms used to solve Maxwell's equations, [35], [36].

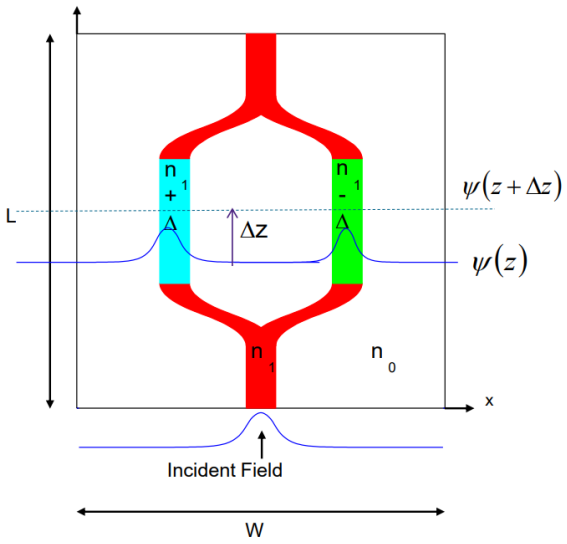

Figure 2.11: Example of BeamPROP simulation, [34].

In this case, in order to check the proper functioning of these MMIs, the simulations consisted of simply generating the structure and exciting it at one input port to check that the output had the same power at both ports. In other words, the MMIs fulfill the function of a 3-dB directional coupler for the entire desired band. For this purpose, the same dimensions of the MMI's multimode waveguide were taken according to GDS file of the design. Different simulations were run, driving the device through its different input ports and measuring its output power.

As shown in Fig. 2.12, the MMI structure has been simulated at three different wavelengths (1550, 1550 and 1600) nm, in order to check the broadband performance of this component through the BPM simulation. For this purpose, the same dimensions have been used as in the device, except that the input and output guides to the device are linear guides instead of curved ones.

The simulations worked well for these wavelengths, as it can be seen how power is split equally through two branches in all cases. So it was decided to carry out a parametric simulation using the multi-variable optimisation tool (MOST) to achieve the same simulation for the band between 1500 and 1600 nm. This tool performs the same simulation in BeamPROP as before but now automatically carries out one for each indicated wavelength. It should be noted that

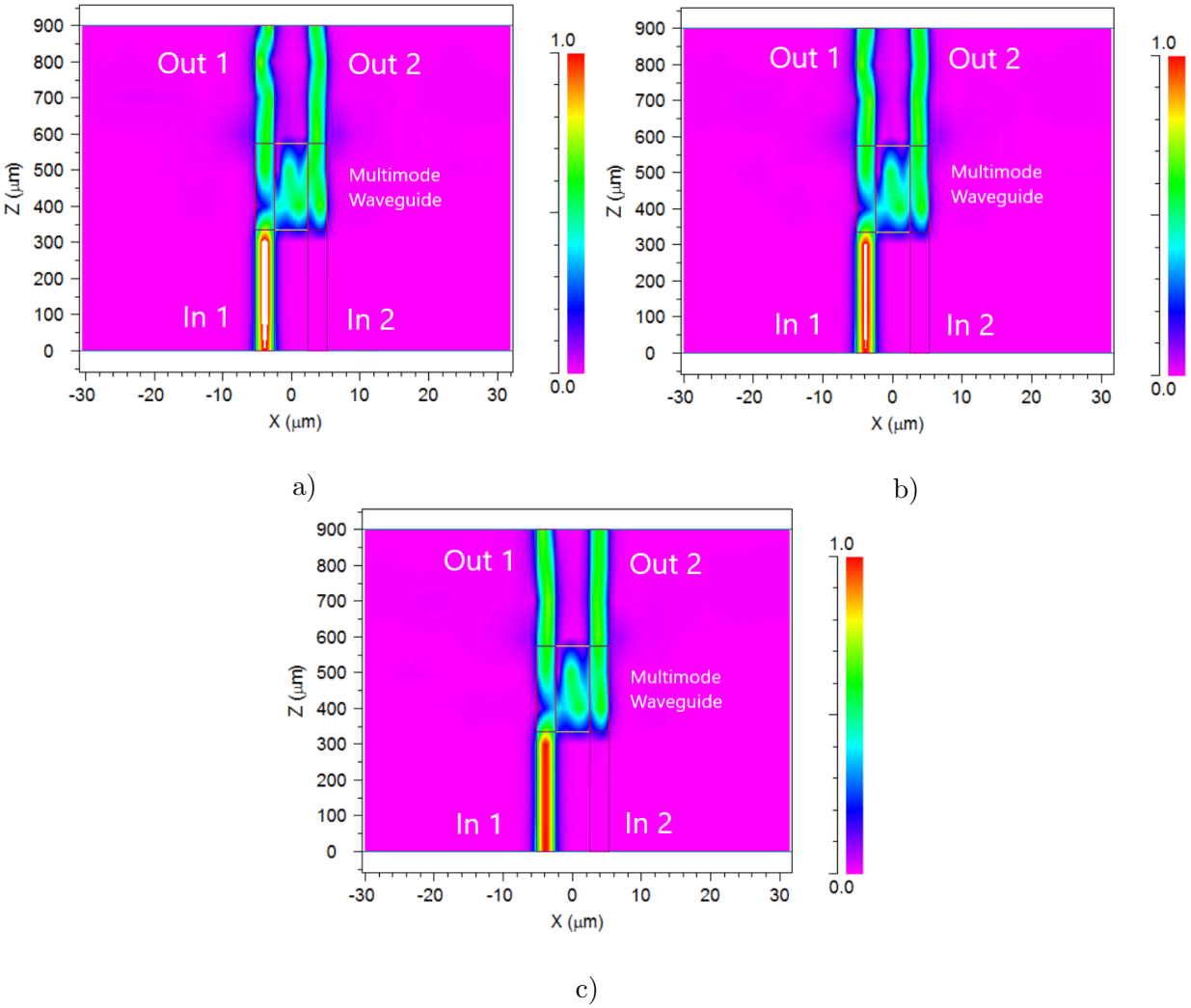

Figure 2.12: a) BeamProp simulation of MMI structure at 1500 nm. b) BeamProp simulation of MMI structure at 1550 nm. c) BeamProp simulation of MMI structure at 1600 nm.

the MOST tool, in this case, has been used for the BeamPROP simulator and the wavelength parameter.

These simulations can be seen after corresponding processing in Fig. 2.13, where the signal responses at the output of the MMI are plotted against the wavelength, for each excitation input port. It can be seen how the spectrum's shape is for each wavelength, particularly seeing how the MMI is optimal in both cases between 1560 and 1600 nm approximately. Despite the difference between the maximum and minimum values over the measured spectrum of approx. 0.8 dB, the good bandwidth performance of this component is remarkable.

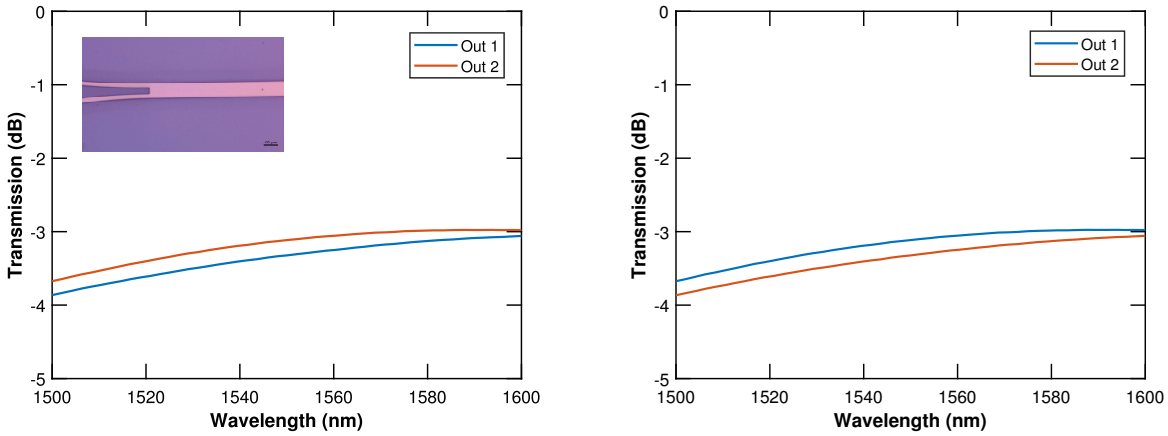

a) b)

Figure 2.13: a) Simulation of the response of the MMI when excited by its input 1. An optical image of the fabricated MMI of a switch system made with *Nikon SMZ800 optical microscope*. b) Simulation of the response of the MMI when excited by its input 2.

2.3.2 Justification of active length

Having explained the most important optical components of the switches to be studied in this work, we will now discuss the electrical part of them. As is well known, these switches work thanks to the thermo-optical effect, which, as explained in previous sections, consists of varying the temperature of the optical waveguide, thereby changing its effective index and thus causing a phase difference between the two branches of the switch and triggering switching.

Therefore, an essential aspect would be the choice of the length of the active part, i.e. the size to which a current will be applied to heat and thereby change the effective index. This involves having to make a trade-off between power consumption and heater resistance since, in principle, it is always sought that this heater length is as small as possible, to achieve a more compact structure. However, this length cannot be made as small as you want. Still, you have to consider that the shorter it is, the more temperature the material must withstand per unit of length, possibly burning if this temperature is too high.

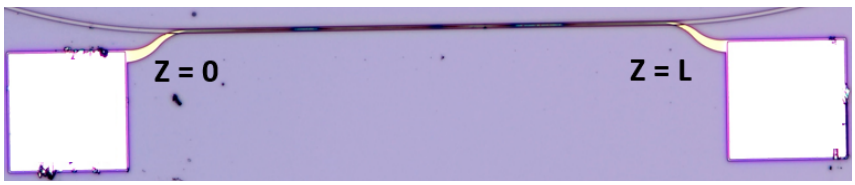

Figure 2.14: Heaters and active part length example. Image of heater structure made with *Nikon SMZ800 optical microscope*.

Thereby, to study the length of the active part, the FemSim tool was used to simulate a variation in n_{eff} based on the change in the index of the silicon nitride waveguide $n_{Si_3N_4}$. Once this relationship has been obtained, the variation of the the effective index Δn_{eff} has been calculated

as a function of the variation of the silicon nitride index $\Delta n_{Si_3N_4}$. And then, using the relationship shown in Eq. 2.1, we have obtained the temperature variation, $\Delta T = (\Delta n_{Si_3N_4})/(2.45 \times 10^{-5})$, that would cause this change of the index in the waveguide. Therefore, we have got the effective index variation as a function of the temperature, as shown in Fig 2.15 b).

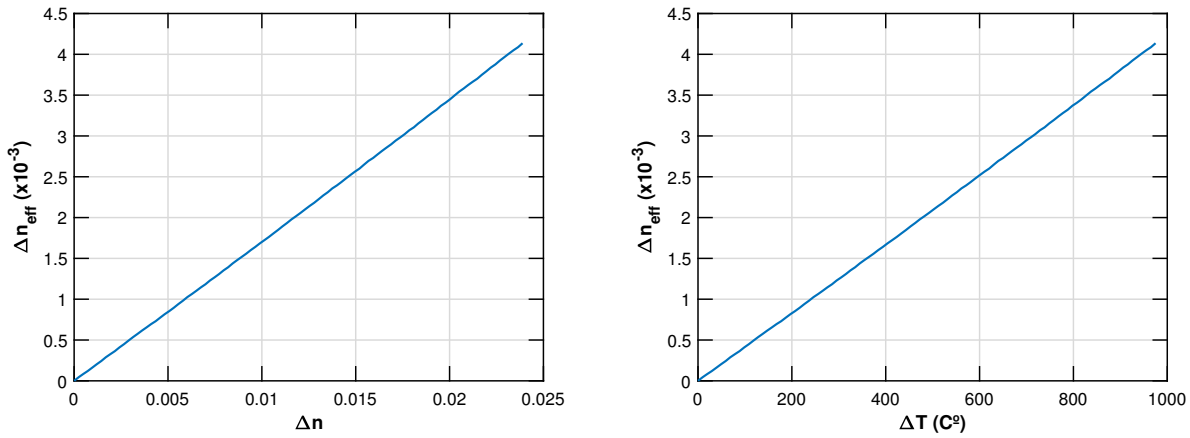

a) b)

Figure 2.15: a) Variation of n_{eff} versus $\Delta n_{Si_3N_4}$, simulated in FemSIM. b) Variation of n_{eff} versus ΔT, calculated by thermo-optic effect equation.

Once the relationships shown in Fig. 2.15 have been established, from Eq. 2.14, the phase difference obtained from the effective index change is mentioned, and the waveguide length for which this phase change is π can be obtained as:

$$\Delta\phi(z = L) = \Delta n_{eff} \frac{2\pi}{\lambda} L = \pi \Longleftrightarrow L = \frac{\lambda}{2\Delta n_{eff}} \tag{2.21}$$

Therefore, the different lengths of the active part required to achieve complete switching can be obtained depending on the temperature that would have to be applied to achieve them, as shown in Fig. 2.16 a). Furthermore, taking into account the active lengths taken for the switches of this design, which are (200, 400, 600, 800, 1000) μm, we have the temperature change necessary to achieve π switching for each length shown in Fig. 2.16 b).

From this Fig. 2.16 a), it can be seen that large footprints in the order of centimeters are needed to achieve π phase shift with small temperature increments. On the other hand, from Fig. 2.16 b), it can be observed that for long lengths of the active part, the local temperature increase that must be applied to these metallic paths is around 200 ºC. However, if you want to reduce the size of the device to 200 μm of the active part, the temperature increase that would have to be made would be much higher, being around 900 ºC, which can be at the limit of damaging the heaters.

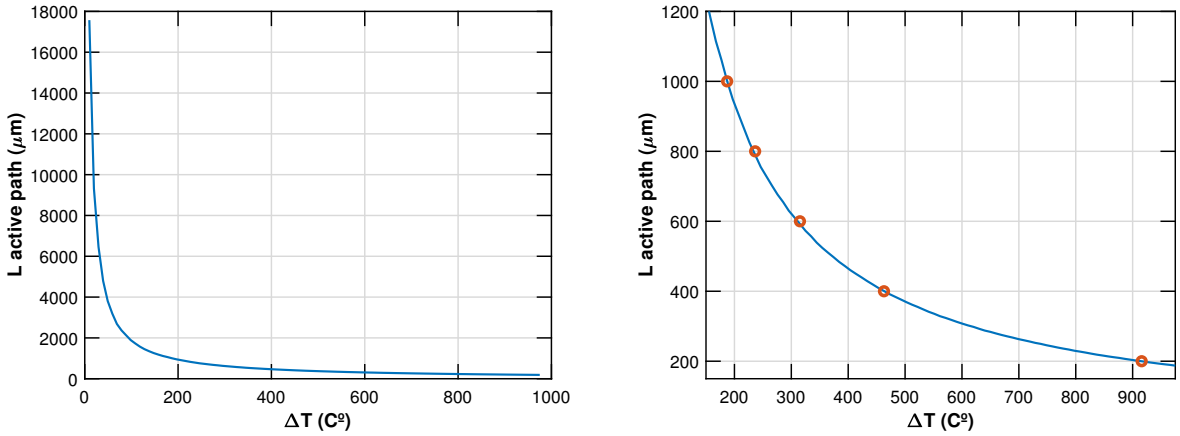

a) b)

Figure 2.16: a) Active path length versus temperature variation to achieve a phase change of π. b) The same graph as in case a) but with zoom focusing on the area where the real lengths of the switches to be studied are given.

2.4 Design of electrodes

This section aims to justify the size and materials chosen for the electrodes of the heaters. This depends on the performance of the heaters to achieve switching, as well as the power consumption of the device. To control the phase change, a thermo-optical tuning based on resistive heating will be used. As it is reported in [37], the optical phase variation related to a temperature change altering the effective refractive index of the waveguide, is given by:

$$\Delta\Phi = \frac{2\pi}{\lambda}\Delta n_{eff} L = \frac{2\pi}{\lambda}\frac{\partial n_{eff}}{\partial T}\Delta T_{wg} L \tag{2.22}$$

Where $\frac{\partial n_{eff}}{\partial T}$ is the TO coefficient that affects the effective refractive index, ΔT_{wg} is the temperature increase in the waveguide and L is the length of the waveguide where ΔT_{wg} is applied. The TO phase shifters use a Joule heat source in the shape of an electrical conductor. The Joule law states that an electrical current, I, through a resistor of resistance R_h, produces heat power proportionally to the square of the current by the resistance of the conductor:

$$P = I^2 R_h \tag{2.23}$$

Therefore, knowing that the electrodes can capture the current and transmit it to the heaters, where the energy has to be dissipated in the form of heat. The electrodes have to be made of a material that is the least resistive possible for this purpose. On the other hand, the heaters have to dissipate as much heat as possible. For this reason, a bi-layer composition of aluminium and titanium (Ti: 100 nm /Al: 150 nm) for the electrodes and a titanium (Ti:100nm) for metal guides have been chosen for the composition of the heaters systems in order to achieve greater dissipation in this part [33]. The scheme is shown in Fig. 2.17.

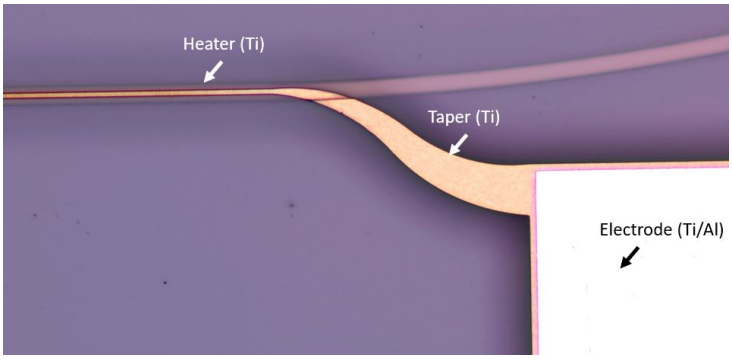

Figure 2.17: Heater material composition. Real image of heater structure made with *Nikon SMZ800 optical microscope*.

As we have seen before, shorter tuners require a higher ΔT_{wg}. However, the thermal energy required is the same as for longer tuners, although more concentrated. Therefore, heat flux is increased. The resistance of the heating element is linearly dependent on the length [37], [38]. It is calculated as follows:

$$R = \rho \frac{L}{S} = \rho \frac{L}{t\ w} \tag{2.24}$$

where ρ is the resistivity in $\Omega \cdot$ m and L, w, t are the length, width and thickness. Whereas the heater consists of two electrodes, two tapers and the heater itself. Considering the pad resistor, has a double metallisation (Ti: 100 nm /Al: 150 nm), can be seen as a parallel resistor ($R_e = R_{Al} \parallel R_{Ti}$). And knowing that the resistivity of the aluminium is an order of magnitude higher than that of titanium, it can be approximated that all the current that will flow through the pad will flow through the aluminium layer (Al: 150 nm). Thereby, ($R_e \approx R_{Al}$), and the calculation of the resistance could be developed as follows:

$$R = 2R_e + 2R_t + R_h = 2\rho_e \frac{L_e}{t_e\ w_e} + 2R_t + \rho_h \frac{L_h}{t_h\ w_h} \tag{2.25}$$

Where e refers to electrodes, t to tapers and h to heaters. As shown in Fig. 2.17, the tapers do not have the shape of a conventional polygon. However, for the calculations of their resistance, their shape will be approximated to that of a trapezoid, as shown in Fig. 2.18. Therefore, their resistance would be:

$$R_t = \rho \frac{L}{S(L)} = \rho \int_0^L \frac{1}{t \cdot w(l)} dl = \frac{\rho}{t} \int_0^L \frac{1}{\frac{W_{end} - W_{ini}}{L} l + W_{ini}} dl = \frac{\rho}{t} \frac{L}{W_{end} - W_{ini}} \ln\left(\frac{W_{end}}{W_{ini}}\right) \tag{2.26}$$

Thereby, operating with the data shown in Fig. 2.18:

$$R_t = \frac{\rho}{t} \frac{55}{10 - 1} \ln\left(\frac{10}{1}\right) \approx 14 \frac{\rho}{t} \tag{2.27}$$

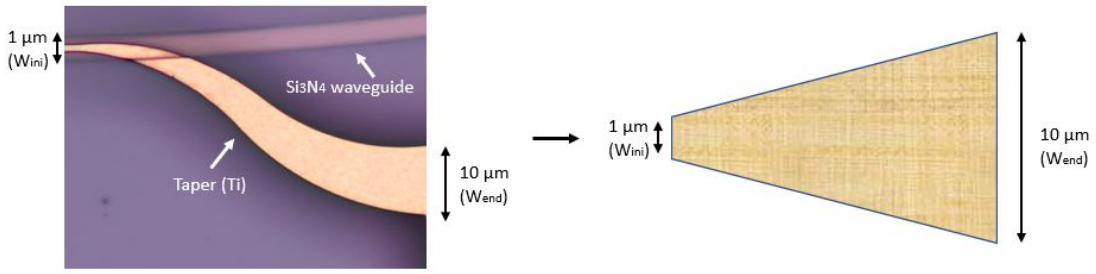

Figure 2.18: Taper form approximation. Image of heater structure made with *Nikon SMZ800 optical microscope*.

So finally the final expression would be:

$$R_{Total} = 2\rho_e \frac{L_e}{t_e\ w_e} + 2 \cdot 14 \frac{\rho_t}{t_t} + \rho_h \frac{L_h}{t_h\ w_h} = 2\rho_e \frac{L_e}{t_e\ w_e} + 28 \frac{\rho_t}{t_t} + \rho_h \frac{L_h}{t_h\ w_h} \tag{2.28}$$

Therefore, $\rho_e = \rho_{Al} = 2.65 \cdot 10^{-8}\ \Omega \cdot m$ and $\rho_t = \rho_h = \rho_{Ti} = 4.2 \cdot 10^{-7}\ \Omega \cdot m$ [39]. Having a pad (electrode) size of 100x100 μm, thereby, $L_e = w_e = 100\ \mu m$. For the width of the heater, $w_h = 1\ \mu m$ shall be taken as indicated in the design. The thicknesses are as described in [3], which states that the aluminium part will have a thickness of 150 nm while the titanium part will be 100 nm. Therefore, $t_e = t_{Al} = 150$ nm and $t_t = t_h = t_{Ti} = 100$ nm. This would result in resistances as a function of heater length, (see Fig. 2.19).

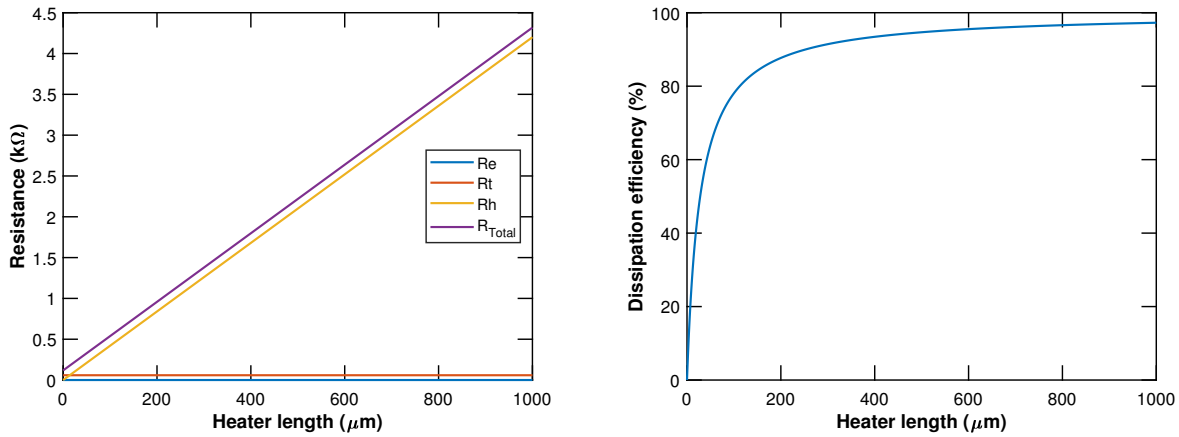

a) b)

Figure 2.19: a) Resistance of each part of complete heater component and resistance of total structure. b) Percentage of heater resistance in the total resistance of the complete structure as a function of heater length.

As shown in Fig 2.19 a), the resistances of the electrodes and tapers, R_e and R_t, are constant and practically do not contribute to the total resistance, especially as the length of the heater increases. On the other hand, there is the heater resistance R_h which, as can be seen, is where most of the energy is dissipated, and as is evident, it grows linearly as the length of the heater

increases. As Fig 2.19 b) shows, from lengths greater than 400 μm, the heater resistance already represents more than 95 % of the total resistance of the device. Therefore, such devices would be of interest to achieve high-efficient systems where heat losses are a critical aspect.

Chapter 3

Switch characterisation

3.1 Introduction

Once the theoretical part has been explained, and the design processes of the integrated switches have been described it is time to test them. This characterisation will be divided into two parts: on the one hand, the main parameters of the switches will be measured, such as IL, crosstalk, power consumption, etc., all depending on the length of the heaters and their distance from the waveguides; this process will be called static characterisation. On the other hand, once the optimum characteristics of those mentioned above are observed as a function of the length and distance of the heater, the switch with the best performance will be chosen to carry out a temporal characterisation with it, in which some parameters will be analysed as a function of time.

Figure 3.1: Diagram in the GDS file of the studied switches.

3.1.1 Si_3N_4 manufacturing process

Speaking of the Si_3N_4 manufacturing process. As mentioned above, the silicon nitride waveguides core usually are fabricated by LPCVD process. According to [40], the waveguide layer is defined by optical projection lithography with an i-line stepper tool and patterned by reactive ion etching (RIE). An optimised RIE process is used that produces steep and smooth sidewalls, which are essential for low-loss operation. After etching, the photoresist mask is removed using an oxygen plasma, and then the LTO cladding material is deposited using LPCVD. Finally, the wafer is annealed at 1000 °C for several hours, which is crucial for improving the quality of the LTO layer and ensuring low-loss operation. Indeed, any high temperature deposition process of high quality SiO_2 should ensure low losses. A description example of fabrication process steps to include the enhanced grating couplers in the ultralow-loss Si_3N_4 waveguide platform is

represented in Fig. 3.2.

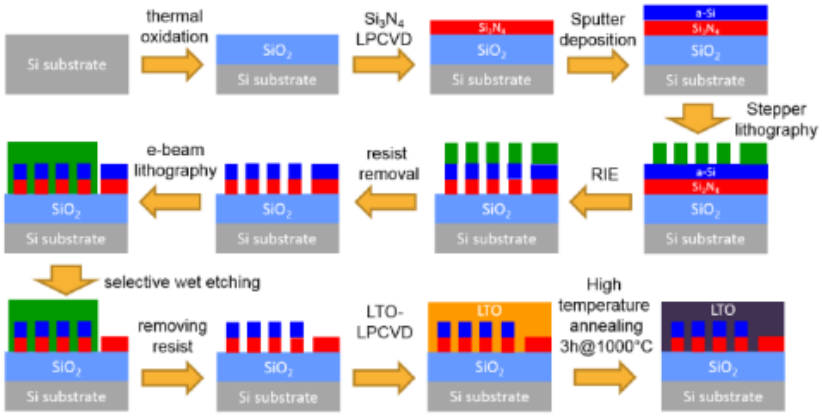

Figure 3.2: Description of fabrication process steps to include the enhanced grating couplers in the ultralow-loss waveguide platform [40].

3.2 Static characterisation

This section intends to study the most important optical parameters of the switches according to their design characteristics. These parameters will be both the IL and the crosstalk to know the losses and the level of the unwanted signal coupled in each case. And the power consumption and Vπ to analyse the performance of the electrical part always depend on the geometrical parameters mentioned.

As can be seen in Fig. 3.1 the switches are arranged as follows on the chip. From left to right, there are five columns of switches, each with a different heater length starting at 1000 μm to the left and decreasing in steps of 200 μm to the right until an active length of 200 μm is reached. Then in each column, the distance between the heater and the optical waveguide varies in each row from 3 μm up to 0 μm the distance of the lowest switch.

3.2.1 Set-up characterisation

First of all, the setup in which the measurements have been taken, has been characterised in order to consider the losses introduced by this to normalise and obtain the results (see Fig. 3.3). It consists of a tunable laser at 1550 nm (*Photonetics ECL-1560*, wavelength range $[1540-1640]$ nm), fibre connectors, a polarisation controller (*FP032, D5 Fiber, FC/APC*, wavelength range $[1260-1625]$ nm), to work only in TE. The coupling of the fibres to the chip is vertical, accessed through the grating couplers. For the coupling, the fibres have an angle of 10 ^{o} concerning the vertical, as shown in Fig. 3.4. Finally, a power meter to record the signal has been used, (*THORLABS PM320E Dual channel optical power meter*, wavelength range $[1260-1625]$ nm, power range $[-70$ to $5]$ dBm). Furthermore of this components, a voltage source (*Keithley* 2440, ± 5.25 A @ ± 10.5 V $||$ ± 1.05 A @ ± 42 V) and a needle probe also have been considered in order to carry out the active measurements to test the electrical performance.

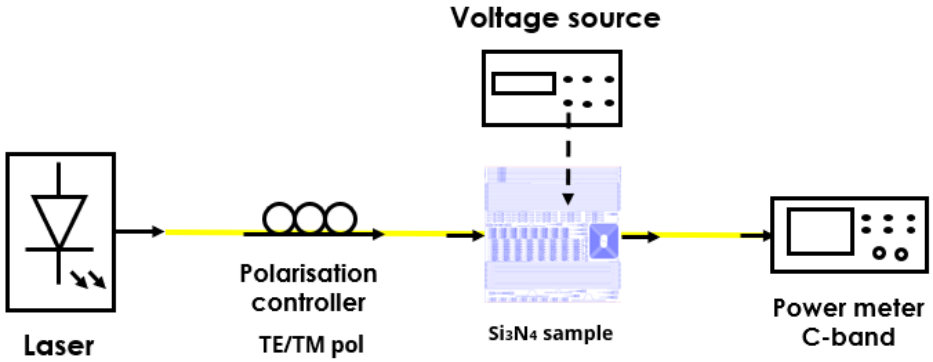

Figure 3.3: Setup diagram to carry out the static characterisation.

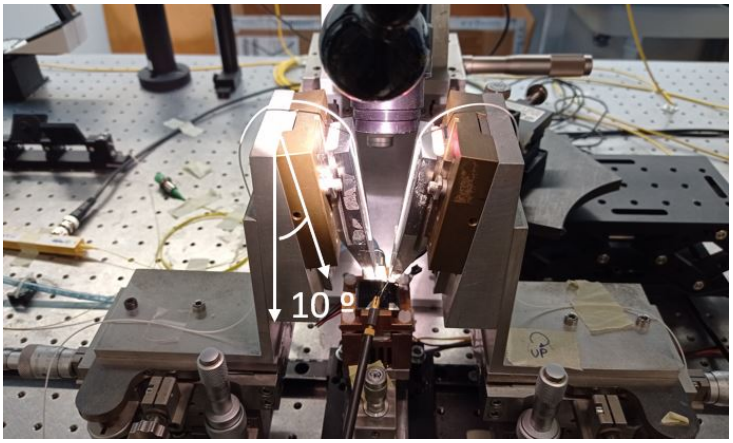

Figure 3.4: Setup used for the characterisation, with the 10 º vertical coupling.

3.2.2 Experimental optical losses

As mentioned above, the main benefit of this technology is the low losses it offers. According to [11], these can be less than 1 dB/m and operate in the 400 to 2350 nm spectrum range. To determine the propagation losses of the fabricated structures, we measured several straight waveguides with different lengths. The length of these waveguides corresponds to the length of the different switches with their distinct lengths of the active part. Hence, the lengths of the measured waveguides are (2445, 2645, 2845, 3045, 3245) μm. The results are shown in Fig. 3.5 a) where the spectra of these guides measured with a continous-wave laser operating in the C- and L-bands [Phototenics ECL-1600] are shown, taking into account the losses of the setup in which they have been measured.

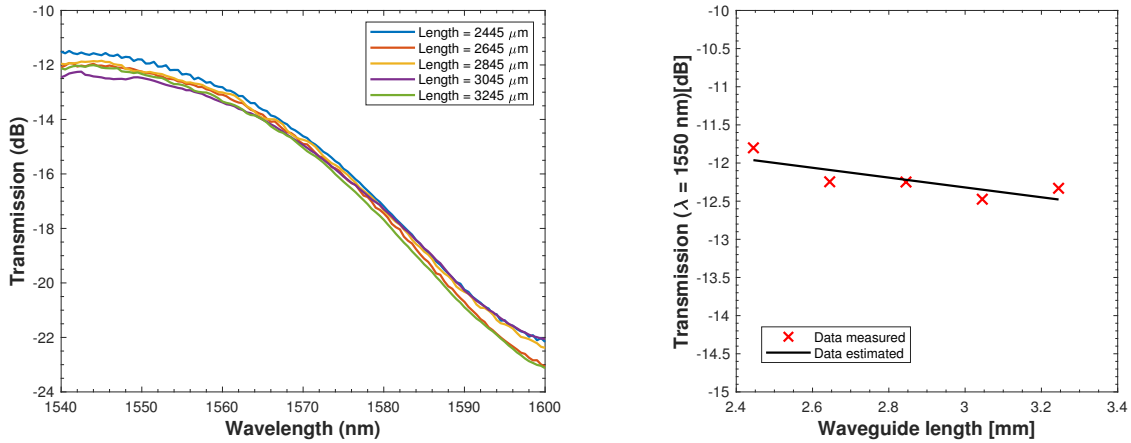

a) b)

Figure 3.5: a) The spectrum of the straight waveguides, with different lengths. Fed with a signal, coming from the laser at a power of 0 dBm. b) Power normalised of waveguides $\lambda = 1550$ nm, with linear fit of losses at this wavelength.

Once the absolute losses of the guides have been represented, in Fig. 3.5 b) an estimation of propagation losses is represented, from waveguide loss data at 1550 nm. However, propagation losses are below the alignment uncertainty (1-2) dB. So it is deduced that virtually all leaks could be attributed to excess losses, which have been estimated and are shown in Fig. 3.6. In this case, these excess losses would correspond to the grating couplers. The graph shows that each grating would have around 5 dB of loss at 1550 nm. Assuming that the spectral response of the grating is symmetrical, its optical bandwidth at 3 dB is 50 nm approx.

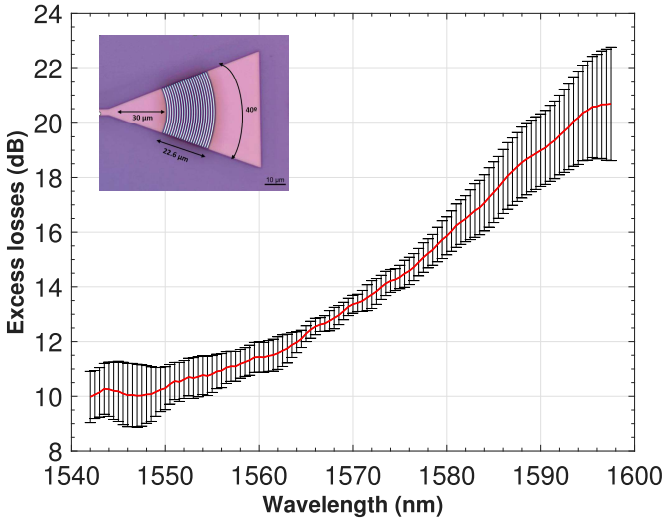

Figure 3.6: Excess losses estimation of the set of waveguides. An optical image of the fabricated focusing grating is depicted in the inset made with *Nikon SMZ800 optical microscope*.

3.2.3 Results and performances

All the switches have been measured to take into account all the lengths of the heaters and all the distances from the heaters to the waveguides in order to carry out a complete practical study, taking into account the IL, the crosstalk, the power consumption and the Vπ.

Insertion losses

Starting with insertion losses, which would be the combination of the propagation losses of the waveguides, and the excess losses, which in this case would be the coupling with the gratings and MMIs. The losses of the switches have been measured, taking the crossed output, i.e. having it in the CROSS state, without applying voltage.

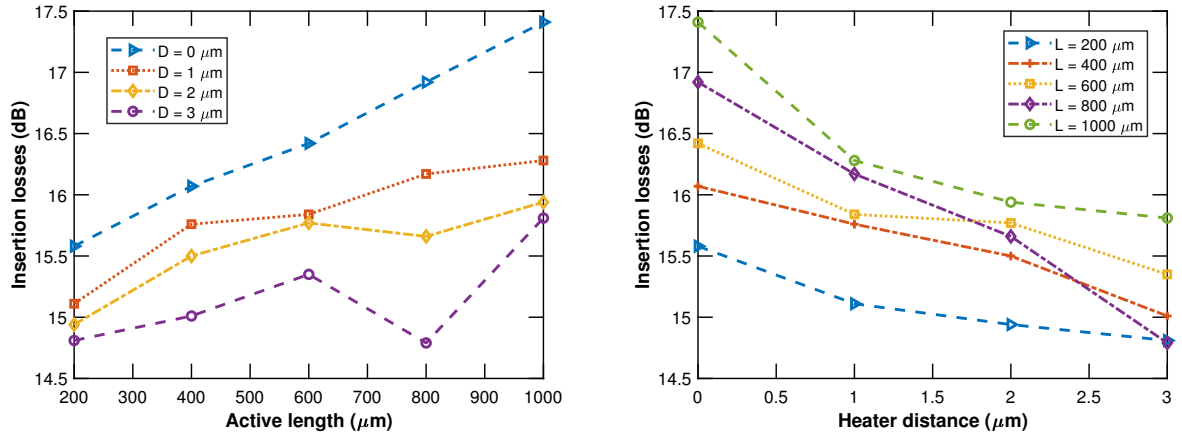

a) b)

Figure 3.7: a) ILs as a function of active length. b) ILs as a function of heater distance. All results are given at $\lambda = 1550$ nm.

Looking at the results in Fig. 3.7 a), it can be seen that the shorter the active length of the pads, the lower the ILs and vice versa. A longer active pad length implies a longer optical waveguide length, which leads to higher propagation losses. On the other hand, with regard to Fig. 3.7 b), it can be seen that the greater the distance between the heater and the optical waveguide, the lower the losses. This is due to the absorption losses in the optical signals when interacting with metals. Hence, the closer the heaters are to each other, the higher the losses. Therefore, in this case, it would be interesting to choose a switch with the shortest possible length and with the greatest distance between the optical waveguide and the heater.

Crosstalk

Moving on to crosstalk, it is used to observe how much of the signal is coupled to the unwanted path, i.e. it takes the other output. Therefore, in this case, we have measured the

power at the output on the same side, being in the CROSS state, without applying any electrical signal.

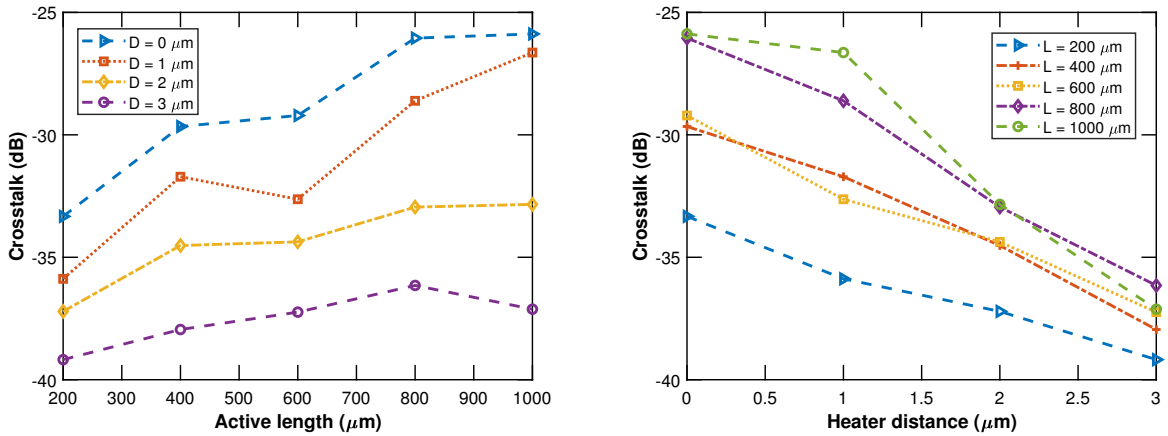

a) b)

Figure 3.8: a) Crosstalk as a function of active length. b) Crosstalk as a function of heater distance. All results are given at $\lambda = 1550$ nm.

Looking at the results of this study (see Fig. 3.8), the same conclusions can be drawn as in the previous case. The shorter the active length and the greater the distance between the heater and the waveguide, the better the performance of the optical part of the system.

Heaters resistance

Once the optical parameters have been dealt with, the electrical part remains to be studied. This section is also critical in most integrated photonic components, as their performance depends partly on it. It starts with the analysis of the heaters resistance so it seems interesting to study this magnitude as a function of heater length experimentally. In order to compare with results of the theoretical study realised in Chapter 2 of this document. Furthermore, also it would be interesting to analyse the dependence of resistance with the electrical power injected.

As it is represented in Fig. 3.9 a), there is some deviation between the measured and theoretically calculated resistance results. The slope values are slightly different, but still close and in the same order of magnitude. This difference could be due to the slight approximations that have been taken for the theoretical calculation, such as the resistivity of the electrodes or the approximation in the shape of the taper. It could also come from slight discrepancies in the real value of the resistivity of the materials and possible slight variations in the thickness of the materials. However, the measured values are in the range estimated by the above calculations.

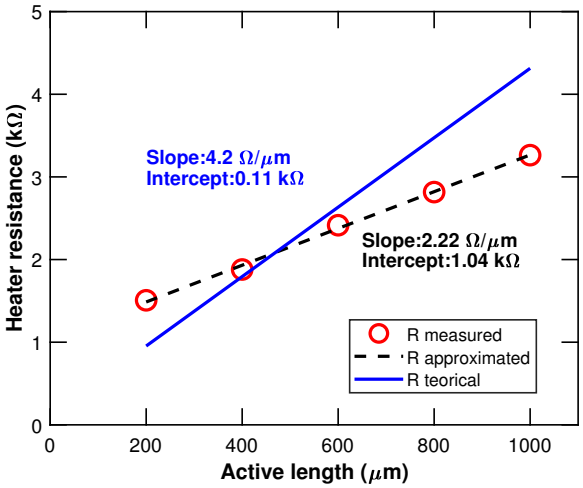

Figure 3.9: Measured heater resistance, measured estimate and theoretical results as a function of active length.

Estimation of Vπ voltage

Another essential electrical parameter is Vπ, which is the voltage that must be applied to the interferometric structure, in this case, the 2x2 switch, to change its phase in π radians. This implies that if this voltage were applied, the signal at the output would not be in the usual CROSS state but would change to the other, going to the BAR state. This parameter is therefore very significant as it indicates the voltage needed to switch and, as can be deduced, the lower, the better, as it is easier to generate lower voltage signals.

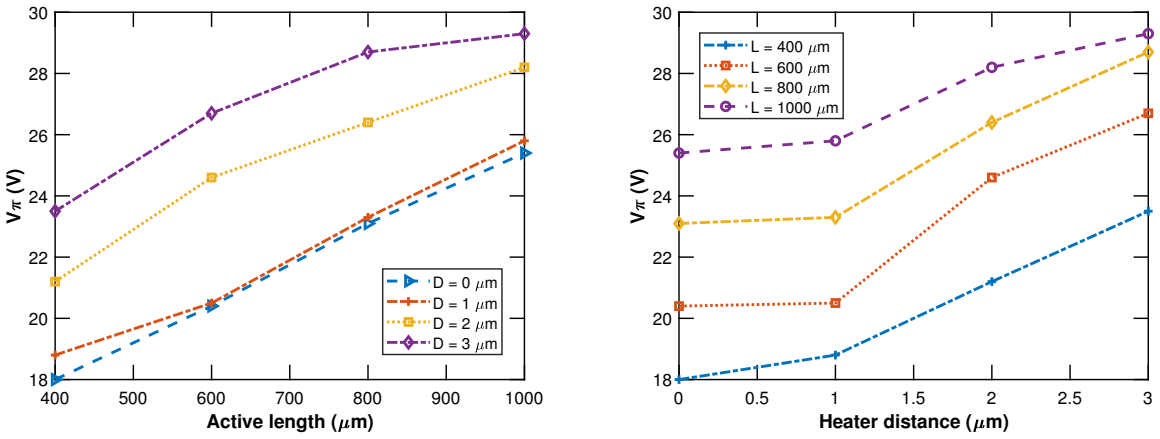

a) b)

Figure 3.10: a) Vπ as a function of active length. b) Vπ as a function of heater distance.

As can be seen in Fig. 3.10 a), a greater length of the active part leads to a higher Vπ, and it is logical that as the length of this part increases, the electrical resistance increases, so a higher voltage is required. And although everything suggests that the shorter the length, the better, it must be considered that this, as mentioned in previous sections, would mean that the heater

would have to withstand a higher temperature per unit length, so there is a trade-off between these parameters. On the other hand, it is also observed that a greater distance between the heater and the optical waveguide implies a greater Vπ, which seems logical. Therefore, in this case, a short length of the active part (as long as the heater holds without burning out) and the smallest possible distance between the heater and the waveguide would be of interest. Note that measures of switches with an active length of 200 μm are not included in these graphs, so their heaters were burned before to reach the Vπ value.

Power consumption

Finally, the last parameter determining the best switch characteristics is power consumption, which can be a critical factor, even more so in integrated circuits in satellite systems. In this case, the results of switches with an active length of 200 μm are not included, for the same reason.

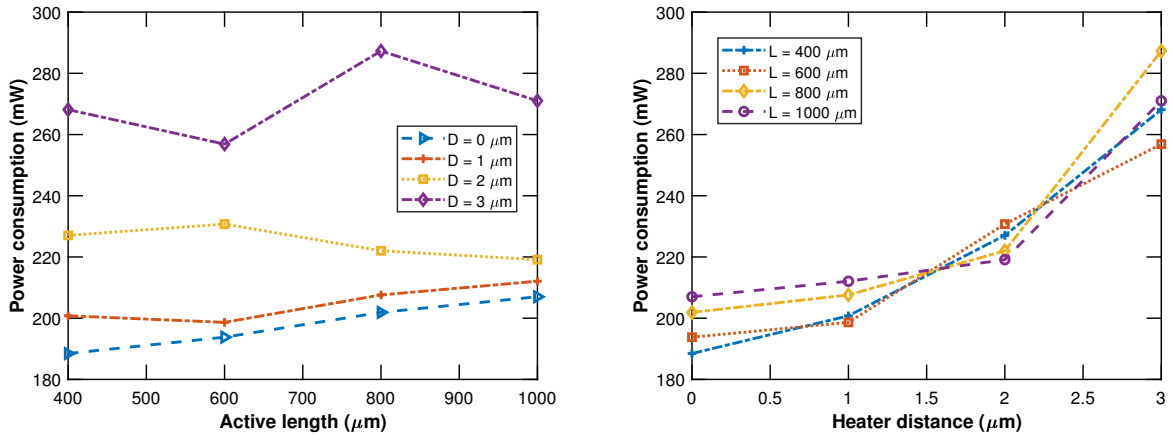

a) b)

Figure 3.11: a) Power consumption as a function of active length. b) Power consumption as a function of heater distance.

Looking at Fig. 3.11, we can see that, as the power consumption is practically independent of the length of the active zone. And although small differences are observed between the values at different lengths, this fact can be attributed to small defects in the heaters. On the other hand, it should be noted how the distance from the heater does affect the power consumption because as the heater distance increases, so does the power consumption. As shown in Fig. 3.11 b), a distance of 3 μm means approximately 80 mW more power consumption compared to having the heater close to the waveguide. This clearly indicates that the switches with the smallest distance between heater and waveguide would have the best electrical performance.

3.2.4 Choice of the best switch

Therefore, considering all the parameters studied, depending on the geometrical characteristics of the switches, the following conclusions are reached. On the one hand, in all cases, the shorter the length of the active part, the better, so it seems logical that the switch chosen should have the shortest possible active length, i.e. 200 μm. However, this will not be possible because all the heaters of these switches burned out, hence the importance of the warning that had already been made previously to keep a trade-off with this length. Therefore, these being discarded, it has been decided to choose a 400 μm active length switch, the next shortest available.

Figure 3.12: Optical image of the switch selected made with *Nikon SMZ800 optical microscope.*

On the other hand, choosing the distance between the heater and the waveguide remains. As we have already seen, there are more doubts in this case because when studying the optical parameters, i.e. IL, it was found that the greater the distance, the better the performance of these parameters. Moreover, the IL improvement when heater distance increases are not so significant for short active lengths, as can be seen in Fig. 3.7 b). However, on the other hand, when studying the electrical parameters, i.e. power consumption, it is observed that a shorter distance is better. Therefore, in this case, we will focus on satisfying the electrical qualities of the switches since reducing the power consumption can be crucial. Thus, the final switch to be studied will be the one with an active length of 400 μm and a distance between the heater and waveguide of 0 μm as Fig. 3.12 shows.

The first step is to represent the spectrum of the switch, using all possible combinations of input and output (following the nomenclature in Fig. 3.12). To do this, the losses of the gratings and the setup will be consigned to normalise the traces and see the real spectrum of the device.

As seen in the spectra representations, good responses are obtained in both the CROSS Fig. 3.13 a) and BAR Fig. 3.13 b) states, as there is a clear difference between the through and non-through paths. In addition, the device performs well in bandwidth, as the measured spectrum response is relatively flat. There is only a difference of about 3 dB between the maximum and minimum values. It is noted that the best performance of the switch is at the 1600 nm wavelength in all cases.

The parameters seen above, such as power consumption and voltage biased, have also been studied further, looking at the optical power in both states and all possible input/output combinations. As shown in the following graphs, where the results are displayed, on the one hand, the power required to achieve complete switching is around 250 mW. On the other hand, the voltage required for switching is around 20 V in both cases.

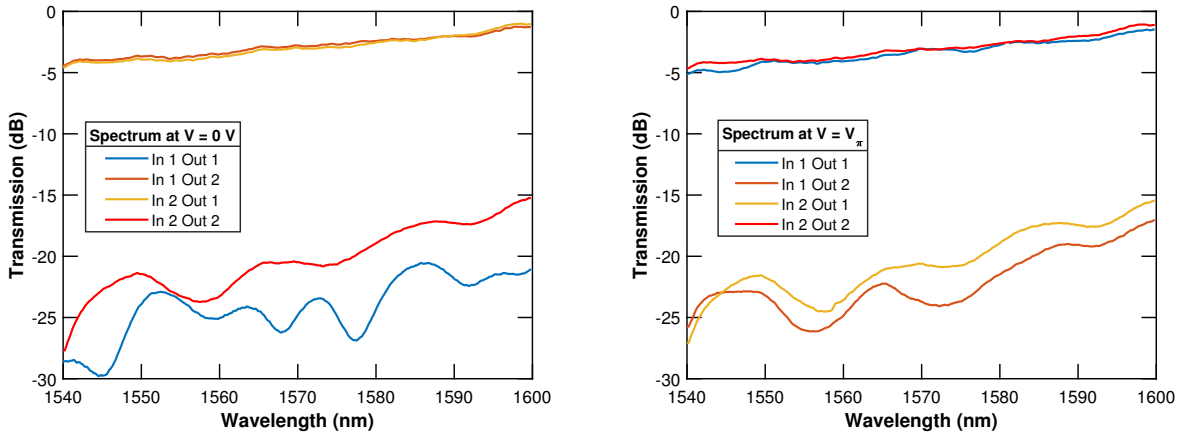

a) b)

Figure 3.13: a) Spectral response of the switch in CROSS state (V = 0 V), with all possible combinations of input and output. b) Spectral response of the switch in BAR state (V = Vπ), with all possible combinations of input and output.

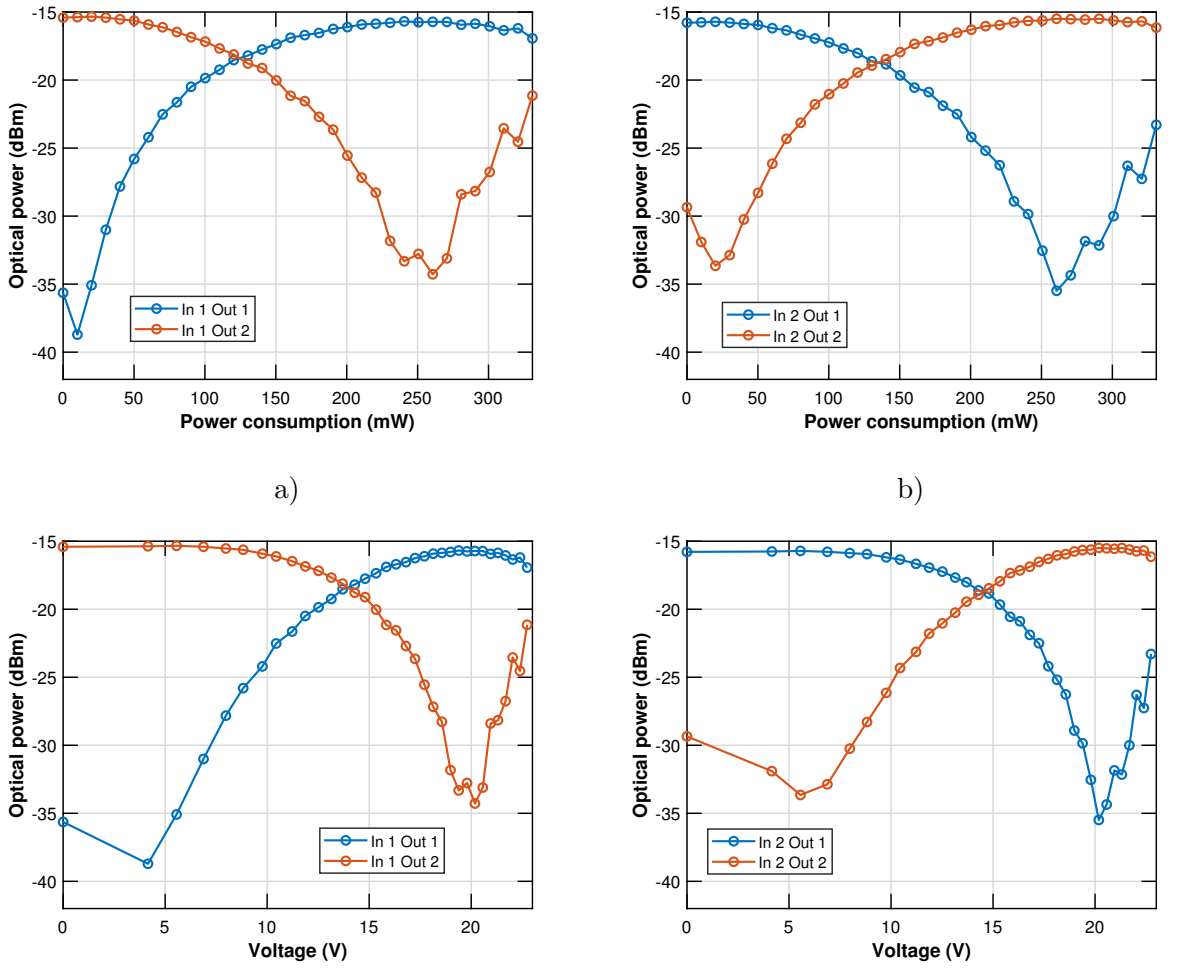

a) b)

c) d)

Figure 3.14: a) Optical power as a function of the switch's power consumption when input one is used. b) Same as a) when input two is used. c) Optical power as a function of the voltage biased when input one is used. d) Same as c) when input two is used. All results are given at $\lambda = 1550$ nm.

3.3 Temporal characterisation

Once the static study has been carried out, the best geometrical properties of the switch are chosen (within certain limitations). We are going to proceed to carry out a temporal study of the selected switch, as the analysis of these parameters is decisive in order to be able to assess the performance of a switch. The parameters to be studied are basically the switching times, specifically, the rise and fall times of the switch response. These are the ones that will ultimately determine the speed at which the switch can operate and, therefore, the rate of the system in which it is implemented.

3.3.1 Set-up characterisation

In order to carry out these measures, a more complex setup was required than the one used for the previous measures. This, as shown in Fig. 3.15, is composed of a tunable laser at 1550 nm (*Photonetics ECL-1560*, wavelength range $[1540-1640]$ nm), fibre connectors, a polarisation controller (*FP032, D5 Fiber, FC/APC*, wavelength range $[1260-1625]$ nm), to work only in TE. The coupling of the fibres to the chip is vertical, as mentioned above, accessed through the grating couplers. For the coupling, the fibres have an angle of 10 º concerning the vertical, as shown in Fig. 3.4. In this case, as the heaters had to be powered for switching, the electrical circuit shown in the schematic of this setup was required. This consists of an arbitrary waveform generator (*Rigol DG1062Z*, amplitude range ($\leq$ 10 MHz) (1 to 10) V_{pp}) to produce square waves. An amplifier module (V_{in} $[0-20]$ V, V_{out} $[0-35]$ V, operation frequency $[0-1.8]$ MHz,) made *ad hoc* to reach signal levels of tens of volts with the signal generated by the waveform generator. In addition, a voltage source (*Keithley* 2440, ± 5.25 A @ ± 10.5 V || ± 1.05 A @ ± 42 V) has been needed to supply the amplifier module. Needle probes were then used to carry the amplified signal to the electrodes of the switches.

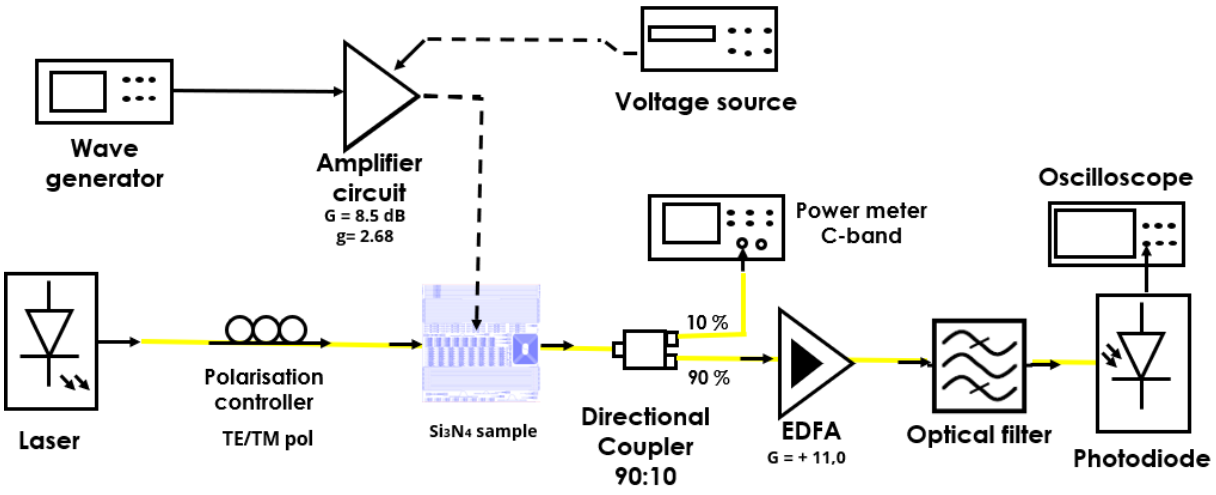

Figure 3.15: Setup diagram to carry out the temporal characterisation.

As the signal levels at the output of the switches were relatively low, higher signal levels are

needed to estimate the switching times. An erbium doped fiber amplifier (EDFA) (*Photonetics*, wavelength range $[1525-1565]$ nm, output power $> +17$ dBm, noise figure < 6 dB) was used to amplify the optical signal. Furthermore, in order to monitor the optical signal at chip output, a directional coupler $(90:10)$ was employed before EDFA. Connecting the derived output to a (*THORLABS PM320E Dual channel optical power meter*, wavelength range $[1260-1625]$ nm, power range $[-70$ to $5]$ dBm) to measure the power. On the other hand, using EDFA generates noise in many parts of the spectrum, so it is also necessary to filter the signal. For this purpose, a tunable filter module holder at 1550 nm (*TFM-1550-S-FA KC-744*, with filter cassette *FC-1565B-1-1* wavelength range $[1545-1565]$ nm, IL ≤ 0.5 dB, FWHM 1 ± 0.2 nm) has been used to keep only the part of the signal we are interested in. In order to detect the final response, the photodetector (*XPDV2120R*, responsivity 0.65 A/W, bandwidth 50 GHz, wavelength range $[1480-1620]$ nm), connected to an oscilloscope (*Rigol scope, DS70034*, 350 MHz, 10 GSa/s, 4 channels), has been used to analyse the signal and extract the parameters of interest.

3.3.2 Results and performances

To evaluate the time performance of the chosen switch, the time response of the switch has been measured using the setup explained in this section (see Fig. 3.15). The aim is to extract the rise and fall times by introducing a (10 V_{pp}, 100 kHz, 50 % duty cycle) signal from the waveform generator, which is amplified. We wanted to study the two switching states (CROOS and BAR), so we characterised the time response of the two possible switch outputs.

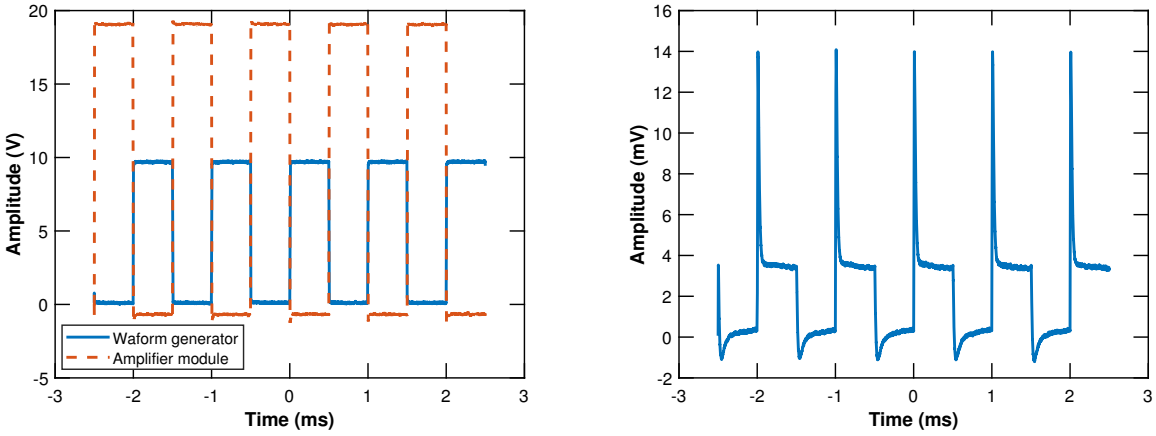

a) b)

Figure 3.16: a) Signal from the waveform generator (10 V_{pp}, 100 kHz, 50 % duty cycle) and signal amplified by the amplifier module. b) Photodetected optical signal.

The results are shown in Fig. 3.16 a), where the responses of both the output of the waveform generator and the amplified signal are represented, as well as the time response of the switch (see Fig. 3.16 b)). Note that the amplifier module reaches a pulse of about 20 V, a value suitable for switching. And the photodetected signal level is around 4 mV. Note also that an unwanted peak is shown in the latter, which according to [41], is due to the fact that slow gain characteristics

of EDFA, which causes saturation and recovery effects in low frequency signals. This is because the input signal is at the upper level during the turn-on time and EDFA needs time to replenish the population by pumping. The gain saturation and recovery effects lead to transients and distortion of the amplified output.

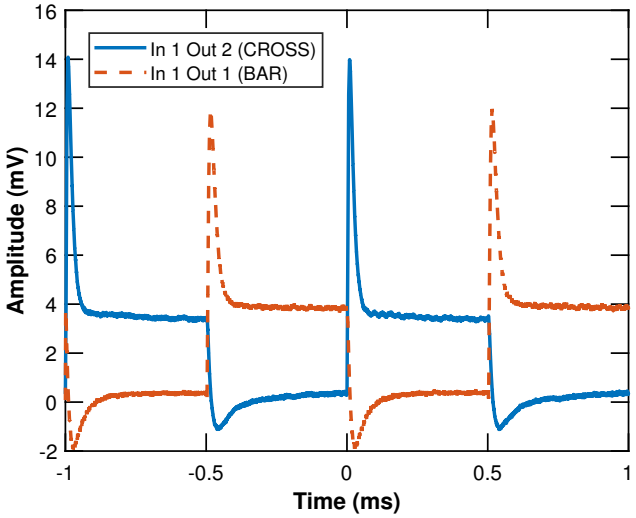

Figure 3.17: Temporal analysis comparison of the switching status.

Furthermore, the pulses in the two possible outputs of the device have been measured in order to test the influence of the switch status (CROSS and BAR) on the time performance. The results are shown in Fig. 3.17, where you can see that both outputs have almost the same signal level. In addition, this new output also suffers from the adverse effect of EDFA distortion.

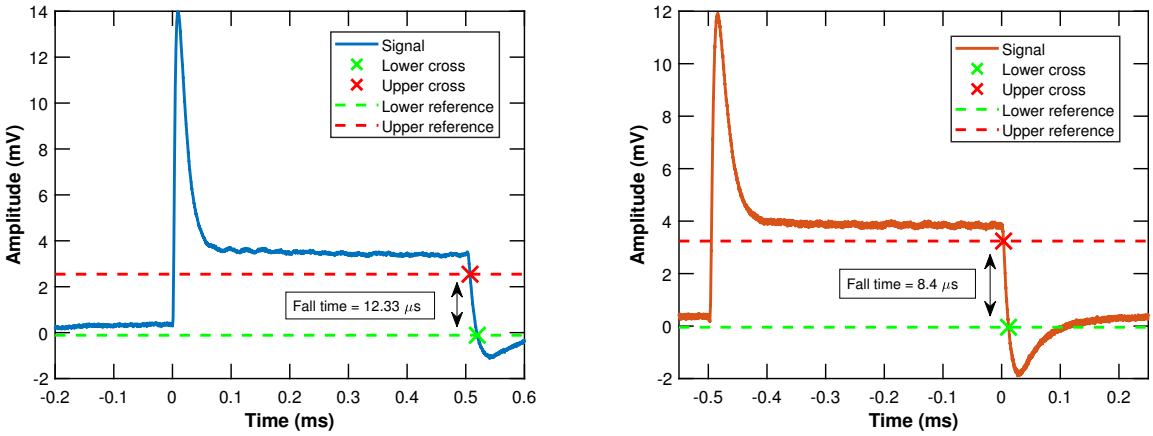

a) b)

Figure 3.18: a) Temporal analysis of one pulse of photodetected optical signal (CROSS state). b) Temporal analysis of one pulse of photodetected optical signal (BAR state).

Finally, a study of the switching times in both states has been carried out. Due to the EDFA transient problem, only the fall time of the pulse has been calculated, as the rise time could

not be properly measured. As Fig. 3.18 a) shows, the result of the fall time is quite reasonable and meets the expected expectations of the device. As reported in [42], the switching times of switches based on the thermo-optical effect are in the order of microseconds.

Chapter 4

Conclusions and future work

4.1 Conclusions

In this Master's thesis, an ultra-low loss optical switch has been demonstrated. This work has been carried out at both the design and characterisation levels to illustrate the operation of the device both theoretically and experimentally.

Starting from the design side, a Si_3N_4 waveguide with an optimised size for ultra-low losses has been used for this project. Compared to a standard silicon waveguide, this offers much lower losses, around two orders of magnitude less, as well as much less dispersion in the desired band. In addition, components that make up the complete switch system, such as the MMIs, have also been studied. In this case, geometrical parameters have been analysed to provide adequate performance in both TE and TM. For TE, more compact designs with the same version have been obtained. However, the device shows outstanding bandwidth performance for both polarisations. On the other hand, a study of how the active length affects to the performance of the device has been carried out. It is clear that the shortest possible length is desired. However, this means that the heater has to withstand a higher temperature which, at a given moment, can cause it to break. Therefore, a balance has to be found to reach the optimum performance point taking both parameters into account.

Next, the electrical behaviour of the heaters has been studied, considering both the electrodes and the tapers as well as the heater itself. In this case, the power distribution between these three parts was analysed depending on the length of the heater in order to observe which lengths would be better for the power distribution to keep a more significant proportion in the heaters and thus make better use of the energy used. This is linked to the heater being as long as possible. But it is also bearing in mind that the heater cannot be as long as you want it to be; the more compact, the better.

In terms of device characterisation, different switches with different geometrical characteristics have been tested, particularly the active length and the distance from the heater. Various optical and electrical parameters have been analysed to determine which switch has the best overall performance. Starting with the IL and crosstalk, it was found that the switches with a

shorter active length and with shortest distance from the heater to the waveguide are the ones that offer the best performance in these parameters. On the other hand, looking at the electrical parameters such as Vπ or the device's power consumption, it is concluded that shorter active lengths and smaller heater distances work better. Therefore, evaluating the results of this static characterisation as a whole, the switch with an active length of 400 μm and a heater distance of 0 μm has been chosen as the best one to study its time response. Furthermore, this switch has been analysed in more detail, and it can be reported that experimentally a Vπ of 20 V and a Pπ of approximately 250 mW are obtained.

Talking about the timing characterisation results, it has been found that the fall times are very similar in the two switching states. These are a few microseconds, a reasonable value for this technology. Finally, it should be noted that the signal rise times could not be measured due to the EDFA saturation problem explained above.

4.2 Future work

To continue along the lines of this project, these photonic components could be assembled and characterised on their new platform. Once they have been verified that are working properly, they could be integrated into the satellite's communication system, for which they have been designed. Other possible future work would be to improve the switch's performance if it were used for other applications. For example, air trenches could be added to the sides to reduce power consumption. However, this would imply a slower operating time, so a suitable balance would have to be found to satisfy both parameters to the extent necessary. Additionally, one could also try to improve the switching times. Although for this work, those obtained are more than sufficient. New applications can always arise that require shorter switching times. Therefore, a study of how the geometrical parameters of the switch affect its time performance could be carried out in order to find the best outcomes.

On the other hand, it would be great if the results and conclusions obtained in this work could be used for further works. These projects could be related to temporal studies based on the thermo-optical effect. Or simply in research involving systems integrated with silicon nitride technology, for which particular simulations carried out in this project could be of benefit. Especially if ultra-low propagation losses are a determining factor in the application in question, as they have been for this project.

Bibliography

[1] Chrostowski, L., & Hochberg, M. (2019). Silicon photonics design. Cambridge: Cambridge University Press.

[2] Sinatkas, G., Christopoulos, T., Tsilipakos, O., & Kriezis, E. (2021). Electro-optic modulation in integrated photonics. Journal Of Applied Physics, 130(1), 010901. doi: 10.1063/5.0048712

[3] Parra, J., Olivares, I., Brimont, A., & Sanchis, P. (2021). Toward Nonvolatile Switching in Silicon Photonic Devices. Laser & Photonics Reviews, 15(6), 2000501. doi: 10.1002/lpor.202000501

[4] Margalit, N., Xiang, C., Bowers, S. M., Bjorlin, A., Blum, R., & Bowers, J. E. (2021). Perspective on the future of silicon photonics and electronics. Applied Physics Letters, 118(22), 220501.

[5] Jalali, B., & Fathpour, S. (2006). Silicon Photonics. Journal Of Lightwave Technology, 24(12), 4600-4615. doi: 10.1109/jlt.2006.885782.

[6] Reed, G., & Knights, A. (2010). Silicon photonics. Chichester: John Wiley.

[7] Debray, A., Malinge, J., & Mounier, E. (2021). Silicon Photonics 2021. Yole Développement.

[8] Baets, R., Subramanian, A., Clemmen, S., Kuyken, B., Bienstman, P., & Le Thomas, N. et al. (2016). Silicon Photonics: silicon nitride versus silicon-on-insulator. Optical Fiber Communication Conference 2016.

[9] Liu, J., Huang, G., Wang, R., He, J., Raja, A., & Liu, T. et al. (2021). High-yield, wafer-scale fabrication of ultralow-loss, dispersion-engineered silicon nitride photonic circuits. Nature Communications, 12(1). doi: 10.1038/s41467-021-21973-z

[10] Chiles, J., & Fathpour, S. (2017). Silicon photonics beyond silicon-on-insulator. Journal of Optics, 19(5), 053001.

[11] Blumenthal, D., Heideman, R., Geuzebroek, D., Leinse, A., & Roeloffzen, C. (2018). Silicon Nitride in Silicon Photonics. Proceedings Of The IEEE, 106(12), 2209-2231. doi: 10.1109/jproc.2018.2861576

[12] Romero-García, S., Merget, F., Zhong, F., Finkelstein, H., & Witzens, J. (2013). Silicon nitride CMOS-compatible platform for integrated photonics applications at visible wavelengths. Optics express, 21(12), 14036-14046.

[13] T. Sharma et al., "Review of Recent Progress on Silicon Nitride-Based Photonic Integrated Circuits," in IEEE Access, vol. 8, pp. 195436-195446, 2020, doi: 10.1109/ACCESS.2020.3032186.

[14] A. Rahim et al., "Open-Access Silicon Photonics Platforms in Europe," in IEEE Journal of Selected Topics in Quantum Electronics, vol. 25, no. 5, pp. 1-18, Sept.-Oct. 2019, Art no. 8200818, doi: 10.1109/JSTQE.2019.2915949.

[15] Muñoz, P., Doménech, J. D., Domínguez, C., Sánchez, A., Micó, G., Bru, L. A., ... & Pastor, D. (2017, July). State of the art of Silicon Nitride photonics integration platforms. In 2017 19th International Conference on Transparent Optical Networks (ICTON) (pp. 1-4). IEEE.

[16] Ciminelli, C., Dell'Olio, F., & Armenise, M. Photonics in space.

[17] Mengual, T., Duarte, V., Polo, V., Piqueras, M., Sanchis, P., & Brimont, A. et al. (2020). Miniaturised photonic front-end for the next generation of space SAR applications. EU-Funded H2020 Project RETINA.

[18] Mengual, T., Duarte, V. C., Polo, V., Piqueras, M. A., Sanchis, P., Brimont, A., ... & Huggard, P. G. (2021, June). Miniaturised photonic front-end for the next generation of space SAR applications. In International Conference on Space Optics?ICSO 2020 (Vol. 11852, pp. 2119-2130). SPIE.

[19] M. Burla, D. Marpaung, L. Zhuang, A. Leinse, M. Hoekman, R. Heideman, and C. Roeloffzen, Integrated photonic Ku-band beamformer chip with continuous amplitude and delay control, IEEE Photon. Technol. Lett. 25(12), 1145?1148 (2013).

[20] Vidal, B., Mengual, T., Ibanez-Lopez, C., & Marti, J. (2006). Optical beamforming network based on fiber-optical delay lines and spatial light modulators for large antenna arrays. IEEE Photonics Technology Letters, 18(24), 2590-2592.

[21] Piqueras, M. A., Mengual, T., Chmielak, B., Catalani, A., Huggard, P., Wang, H., & Ortuño, R. (2015, September). Photonic front-end for the next-generation of space SAR applications. In 2015 10th European Microwave Integrated Circuits Conference (EuMIC) (pp. 301-304). IEEE.

[22] A. Meijerink, C. G. H. Roeloffzen, R. Meijerink, L. Zhuang, D. A. I. Marpaung, M. J. Bentum, M. Burla, J. Verpoorte, P. Jorna, A. Hulzinga, and W. C. van Etten, Novel ring resonator-based integrated photonic beamformer for broadband phased-array antennas-Part I: design and performance analysis, J. Lightwave Technol. 28(1), 318 (2010).

[23] L. Zhuang, C. G. H. Roeloffzen, A. Meijerink, M. Burla, D. A. I. Marpaung, A. Leinse, M. Hoekman, R. G. Heideman, and W. C. van Etten, Novel ring resonator-based integrated photonic beamformer for broadband phased-array antennas-Part II: experimental prototype, J. Lightwave Technol. 28(1), 1931 (2010).

[24] Brimont, A., Zurita, D., Duarte, V., Mengual, T., Chmielak, B., & Suckow, S. et al. (2020). Optical fiber-to-chip assembly process for ultra-low loss photonic devices based on silicon nitride for space applications. EU-Funded H2020 Project RETINA.

[25] Singh, G., Yadav, R. P., Janyani, V., & Ray, A. (2008). Design of 2x2 optoelectronic switch based on MZI and study the effect of electrode switching voltages. Journal of World Academy of Science, Engineering and Technology, 39, 401-407.

[26] Kasper, E., & Yu, J. (2020). Silicon-Based Photonics (1st ed.). Jenny Stanford Publishing. https://doi.org/10.1201/9781315156514.

[27] Cocorullo, G., Della Corte, F. G., Rendina, I., & Sarro, P. M. (1998). Thermo-optic effect exploitation in silicon microstructures. Sensors and Actuators A: Physical, 71(1-2), 19-26.

[28] Pitilakis, A., & Kriezis, E. E. (2011). Longitudinal 2 x 2 switching configurations based on thermo-optically addressed dielectric-loaded plasmonic waveguides. Journal of lightwave technology, 29(17), 2636-2646.

[29] Su, Y., Zhang, Y., Qiu, C., Guo, X., & Sun, L. (2020). Silicon photonic platform for passive waveguide devices: Materials, fabrication, and applications. Advanced Materials Technologies, 5(8), 1901153.

[30] Arbabi, A., & Goddard, L. L. (2013). Measurements of the refractive indices and thermo-optic coefficients of Si 3 N 4 and SiO x using microring resonances. Optics letters, 38(19), 3878-3881.

[31] Sanchis, P., Basic structures in photonic integrated circuits. Nanophotonics. Course 2020-2021.

[32] Soldano, L. B., & Pennings, E. C. (1995). Optical multi-mode interference devices based on self-imaging: principles and applications. Journal of lightwave technology, 13(4), 615-627.

[33] Piqueras, M. A., RETINA, Miniaturised photonics enabled next generation SAR. [Online]. Available: https://www.dasphotonics.com/proyectos/

[34] Synopsys, RSoft package. [Online]. Available: https://www.synopsys.com/photonic-solutions.html

[35] Xu, C., Heller, E., Bahl, M., Scarmozzino, R., Ku, K. N., Zhou, Y., ... & Lin, C. C. (2021, December). Suitability of BPM Simulation for Silicon Photonics. In 2021 IEEE 17th International Conference on Group IV Photonics (GFP) (pp. 1-2). IEEE.

[36] Chang, P. C., Lin, C. Y., Chen, S. C., Wang, C. L., & Lin, C. C. Suitability of BPM Simulation for Silicon Photonics.

[37] Alemany, R., Muñoz, P., Pastor, D., & Domínguez, C. (2021, November). Thermo-Optic Phase Tuners Analysis and Design for Process Modules on a Silicon Nitride Platform. In Photonics (Vol. 8, No. 11, p. 496). Multidisciplinary Digital Publishing Institute.

[38] Pérez, D., Fernández, J., Baños, R., Doménech, J. D., Sánchez, A. M., Cirera, J. M., ... & Munoz, P. (2016). Thermal tuners on a Silicon Nitride platform. arXiv preprint arXiv:1604.02958.

[39] Dyos, G. (2012). The Handbook of Electrical Resistivity: New materials and pressure effects. The Institution of Engineering and Technology.

[40] Chmielak, B., Suckow, S., Parra, J., Duarte, V. C., Mengual, T., Piqueras, M. A., ... & Sanchis, P. (2022). High-efficiency grating coupler for an ultralow-loss Si3N4-based platform. Optics Letters, 47(10), 2498-2501.

[41] Meena, D., Sarath, K. T., Francis, F., Dipin, E., & Srinivas, T. (2019). Mitigation of EDFA transient effects in variable duty cycle pulsed signals. Defence Technology, 15(3), 276-281.

[42] Yao, Y., Cheng, Z., Dong, J., & Zhang, X. (2020). Performance of integrated optical switches based on 2D materials and beyond. Frontiers of Optoelectronics, 13(2), 129-138.